Spectrochimica Acta Part B 82 (2013) 1–27

Contents lists available at SciVerse ScienceDirect

Spectrochimica Acta Part B

journal homepage: www.elsevier.com/locate/sab

Pre-flight calibration and initial data processing for the ChemCam laser-induced breakdown spectroscopy instrument on the Mars Science Laboratory rover

R.C. Wiens [a,*], S. Maurice [b], J. Lasue [b], O. Forni [b], R.B. Anderson [c], S. Clegg [a], S. Bender [d], D. Blaney [e], B.L. Barraclough [d], A. Cousin [a,b], L. Deflores [e], D. Delapp [a], M.D. Dyar [f], C. Fabre [g], O. Gasnault [b], N. Lanza [a], J. Mazoyer [h], N. Melikechi [i], P.-Y. Meslin [b], H. Newsom [j], A. Ollila [j], R. Perez [k], R.L. Tokar [d], D. Vaniman [d]

[a] Los Alamos National Laboratory, Los Alamos, NM 87544, USA
[b] Institut de Recherche en Astrophysique et Planetologie, Toulouse, France
[c] United States Geological Survey, Flagstaff, AZ, USA
[d] Planetary Science Institute, Tucson, AZ, USA
[e] Jet Propulsion Laboratory, Pasadena, CA, USA
[f] Mount Holyoke College, South Hadley, MA, USA
[g] Georessources, Nancy, France
[h] LESIA, Observatoire de Paris, Meudon, France
[i] Delaware State University, Dover, DE, USA
[j] University of New Mexico, Albuquerque, NM, USA
[k] Centre Nationale d'Etude Spatiale, Toulouse, France

ARTICLE INFO

Article history:
Received 11 January 2013
Accepted 6 February 2013
Available online 18 February 2013

Keywords:
Laser-induced breakdown spectroscopy
LIBS
Mars
Curiosity rover
ChemCam

ABSTRACT

The ChemCam instrument package on the Mars Science Laboratory rover, Curiosity, is the first planetary science instrument to employ laser-induced breakdown spectroscopy (LIBS) to determine the compositions of geological samples on another planet. Pre-processing of the spectra involves subtracting the ambient light background, removing noise, removing the electron continuum, calibrating for the wavelength, correcting for the variable distance to the target, and applying a wavelength-dependent correction for the instrument response. Further processing of the data uses multivariate and univariate comparisons with a LIBS spectral library developed prior to launch as well as comparisons with several on-board standards post-landing. The level-2 data products include semi-quantitative abundances derived from partial least squares regression.

A LIBS spectral library was developed using 69 rock standards in the form of pressed powder disks, glasses, and ceramics to minimize heterogeneity on the scale of the observation (350–550 μm dia.). The standards covered typical compositional ranges of igneous materials and also included sulfates, carbonates, and phyllosilicates. The provenance and elemental and mineralogical compositions of these standards are described. Spectral characteristics of this data set are presented, including the size distribution and integrated irradiances of the plasmas, and a proxy for plasma temperature as a function of distance from the instrument. Two laboratory-based clones of ChemCam reside in Los Alamos and Toulouse for the purpose of adding new spectra to the database as the need arises. Sensitivity to differences in wavelength correlation to spectral channels and spectral resolution has been investigated, indicating that spectral registration needs to be within half a pixel and resolution needs to match within 1.5 to 2.6 pixels. Absolute errors are tabulated for derived compositions of each major element in each standard using PLS regression. Sources of errors are investigated and discussed, and methods for improving the analytical accuracy of compositions derived from ChemCam spectra are discussed.

1. Introduction

The ChemCam instrument suite was selected to be the remote sensing composition facility for the Mars Science Laboratory (MSL) rover. ChemCam consists of a remote micro-imager (RMI), capable of ~50 mrad resolution, and the first remote laser-induced breakdown spectrometer (LIBS) to be sent to another planet, capable of determining elemental compositions of rocks and soils within 7 m of the instrument [1,2]. The ChemCam LIBS instrument was selected for its ability to actively remove dust and coatings or weathering rinds from rocks to determine their underlying composition, and also for its ability to analyze potential coatings and rinds themselves. Another advantage of LIBS is its ability to rapidly detect many elements, including the light elements H, Li, Be, B, C, N, and O.

* Corresponding author. Tel.: +1 505 667 3101.
E-mail address: rwiens@lanl.gov (R.C. Wiens).

0584-8547 Published by Elsevier B.V. Open access under CC BY-NC-ND license.
http://dx.doi.org/10.1016/j.sab.2013.02.003

LIBS applications have increased over the last 20 years with the advent of miniaturized fiber-optic spectrometers and lasers (e.g., [3,4]). LIBS involves focusing a pulsed laser beam with an irradiance of at least 10 MW/mm^2 onto a solid, liquid, or gaseous target. The intense photon flux breaks down the target material resulting in a plasma. The excited electronic states in the plasma emit light at characteristic wavelengths, resulting in a strong glow that lasts several microseconds [5]. Collection and spectral dispersion of the light allow detection and calibration of the elemental abundances of the target. On solid targets each laser pulse excavates a small distance into the target. Multiple laser pulses at the same location can be used to depth profile into a sample; in the case of ChemCam, depths of 0.5 mm into rock targets have been achieved with 500 laser shots [1]. LIBS spectral line intensities are affected by the atmosphere in which the plasma is produced. Knight et al. [6] showed that at the reduced pressure corresponding to the Mars atmosphere LIBS spectral line intensities are stronger than at terrestrial surface pressures, and the continuum background, line broadening, and self-absorption are all reduced, facilitating simpler LIBS analyses for Mars conditions. For example, the precise time-gating of the detector that is often used to reduce these features in LIBS spectra under terrestrial conditions is not necessary in the Mars environment.

Quantitative LIBS analyses of complex matrices such as geological samples have been hampered by chemical matrix effects, in which the presence of some element, even a minor or trace element, affects the relationship between concentration and emission line intensity of other elements. Matrix effects can be related to differences in coupling efficiency of the laser to the material, or they can be caused by phenomena in the plasma phase, such as the quenching of electronic states and temperature-affecting phenomena [7]. Several approaches have been taken to reduce this problem. One approach, called calibration-free (CF) LIBS, e.g., [8–10], assumes a local thermodynamic equilibrium in the plasma and attempts to solve the Saha equation for all prominent lines of the elements present. CF LIBS has been studied quite extensively and is relatively successful in that quantitative abundances with relative accuracies averaging ±15–20% are achieved on some matrices with no calibration standards whatsoever. The CF LIBS method requires that the plasma temperature be accurately determined, which requires that the electron density be closely estimated, and that a large fraction of all emission lines be observed for each element. The ChemCam spectrometer was not designed to be comprehensive in observing all emission lines from enough elements to make this a feasible approach.

Another approach to chemical matrix effects involves using calibration standards covering the possible range of compositions of the samples of interest and relying on multivariate analysis to correct for the matrix effects. Multivariate analyses can utilize all available spectral channels, rather than one or two emission lines, to produce a correlation model fitting the multi-channel data with a number of standards. The correlation model for a given element commonly has both positive and negative correlations. Channels that have significant correlation factors but do not correspond to an emission line of the element in question represent corrections for a chemical matrix effect as well as geochemical affinities in which the abundance of one element trends with that of another. The latter effect can aid in determining the abundance of the element in question, but care must be taken that the model does not over-emphasize the influence of elements with strong geochemical affinities over emission from the element in question, as correlations based on geochemical affinities can be far from exact in unusual samples. Moreover, trace element abundances predicted purely by geochemical affinities based on abundances in terrestrial standards may not be relevant for Mars. A number of studies using partial least squares (PLS) of principal components have shown the success of this method for major and strongly emitting minor and trace elements in geological samples [11–17]. However, less complex methods such as univariate analyses still have their place, particularly in quantifying elements characterized by weak spectral peaks that would be overlooked, and might have negligible influence relative to the stronger peaks of other elements.

In addition to chemical matrix effects, another factor that must be considered for ChemCam is that of sample-to-instrument distance. As a near-range remote-sensing instrument, the conditions of the laser beam vary, with the focused beam spreading farther at longer distances, leading to differential plasma conditions. Eventually, at great enough distances, the energy density becomes too weak to produce detectable plasma. A significant effort is being made to understand how to produce distance corrections to the signal so that calibrations at one distance will suffice for a sample at a different distance.

This paper provides a comprehensive view of the pre-delivery calibrations undertaken with the ChemCam LIBS instrument and outlines the strategy determining elemental compositions from LIBS spectra. We first give a short description of the instrument and the experimental conditions under which the calibrations were done. A comprehensive description of the standard set is provided. The LIBS plasma size at Mars pressure is presented, along with emission line irradiances and detection limits for emission lines observed by ChemCam under various conditions. Following this, the data treatment methods are described for quantitative calibration using PLS. Finally, the discussion concludes with a short summary of strategies for analyses on Mars and an initial univariate view of the first data taken on Mars of the onboard calibration targets.

An overview of the general multivariate calibration plan is shown in Fig. 1. Standards of known composition were selected during the instrument development time period. LIBS spectra were acquired prior to delivery of the instrument to the rover. These spectra were pre-processed through a number of steps to produce a database from which multivariate training models can be made. Spectra obtained on Mars, indicated in the bottom row, are also pre-processed using exactly the same routines. The team must consider any potential changes to the instrument response on Mars, and must also normalize the spectra to correct for the effects of variable distance. The multivariate training model built on the pre-delivery spectra mentioned above is applied to the Mars spectra to determine their elemental abundances and uncertainties, and to classify the spectra. Classification can also be done purely among Mars samples without referring back to terrestrial standards, and this is useful, for example, in determining differences in regional soil compositions or other changes in Mars samples. Classification can also be done in comparison to terrestrial rock samples for which precise elemental composition is unknown. This can be beneficial in observing the spread in spectral phase space.

A drawback of the model described so far is the limitations of the standards available prior to instrument delivery. It was impossible to accurately anticipate the composition of the Gale Crater samples prior to landing there. For this reason, it is important to have the capability to analyze additional standards using laboratory instruments that are sufficiently similar to ChemCam. This is represented in the middle row of Fig. 1. Before accepting standards from laboratory instruments into the ChemCam multivariate training database, a rigorous comparison must be done between spectra taken by ChemCam on standards that were available prior to delivery, with spectra of the same standards taken with laboratory instruments, to ensure that these new spectra match those from ChemCam in terms of resolution, wavelength, spectral range, and plasma temperature (ratios of peak heights for a given composition). The discussion of data processing will follow the different elements in the figure. The accuracy of the model is quantified by performing leave-one-out analyses on the pre-delivery spectral database.

2. Experimental

2.1. Instrument and experimental layout

The ChemCam instrument is described in detail in two separate papers [1,2]. Briefly, it utilizes a passively-cooled diode-pumped Nd:

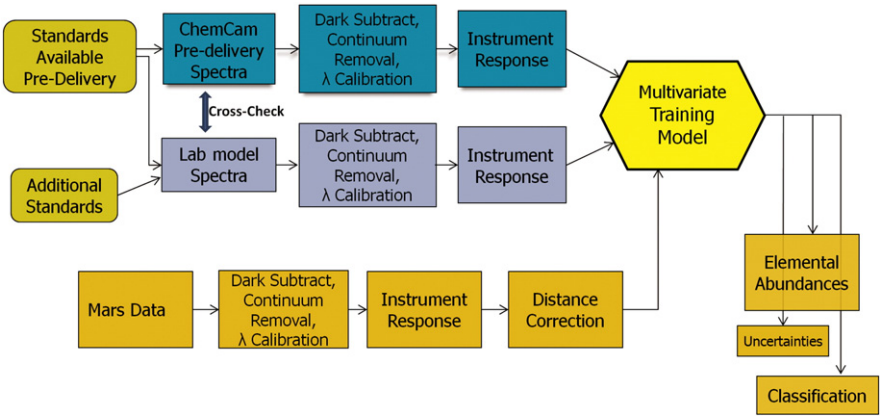

Fig. 1. Multivariate calibration scheme for ChemCam LIBS. The top row represents calibration done on the flight instrument prior to delivery and launch; the bottom row represents input of Mars spectra, which uses a multivariate training model to determine elemental abundances and their uncertainties, and to classify the samples. The middle row indicates the injection of additional training spectra using laboratory-based instruments.

KGW laser with two amplifier slabs to produce 5 ns pulses of 1067 nm photons with energies up to 35 mJ at the laser. The laser system, designed and built by CNES and Thales Optronics, generates a beam that is expanded through a 110 mm diameter Schmidt–Cassegrain telescope to produce a focused spot on targets. The maximum beam energy depends on the temperature of the laser, which was optimized for cool conditions. Between −10 and +10 °C it can reach 14 mJ on target, while at room temperature the maximum is ~10 mJ. The laser energy can be reduced by decreasing the current to the amplifier diode stack below the nominal value of 95 A. For example, at 60 A, the maximum laser energy, when cooled, is ~9 mJ, and at 40 A it is ~6.5 mJ. The same telescope is used to send the laser beam and also collect the plasma light, launching it into an optical fiber leading to a demultiplexer and three spectrometers covering 240–850 nm except for a gap from 340–385 nm. The spectrometers, referred to as UV, violet (VIO), and visible and near-infrared (VNIR) are relatively simple crossed Czerny–Turner designs using spherical mirrors that produce a spread of up to 2 mm in the spatial direction but that have a resolution of 2.5–5 pixels full-width half-maximum (FWHM) spectrally. The detectors are three e2v 42-10 back illuminated CCDs operated in advanced inverted mode, each having 2048×512 pixels, each 13.5 μm square.. For LIBS the spectra are collapsed to 1D on chip, typically integrating 200 pixels in the spatial dimension to cover the beam spread. Integration times are approximately 10 ms, which is long compared to the duration of the plasma, on the order of 10 μs.

A number of different experimental arrangements [1] were used to obtain the data reported here. Table 1 gives an overview of the various conditions for the different experiments. The conditions that were varied include sample distance (1.58, 3.0, 5.0, 7.0, 8.7 m), laser amplifier diode stack current, which controls the output energy, the number of laser shots and depth into the sample, temperature of the instrument, surface obscuration by dust, soil vs. solid samples, and sample composition. Most tests were performed in a chamber containing 930±130 Pa of CO_2, however, some tests were carried out at either terrestrial atmospheric pressure or at Mars pressure (930 Pa) using terrestrial air composition. The main portion of this paper will deal with Test #6 in Table 1, during which spectra were obtained from 69 geological standards at a distance of 3.0 m. In this and several other tests, 40–50 spectra were obtained from each of the four observation points per standard at a sampling rate of 3 Hz. The data processing applied to these spectra is described below.

Data on plasma diameters were taken using laboratory equipment. These measurements were made during the design phase of ChemCam to determine the field of view needed to capture all of the available LIBS light. This portion of the experiment used a Spectra-Physics Indi Nd:YAG laser operating at 1064 nm with a 10 ns pulse with 17±1 mJ energy measured outside the sample chamber, as described in Clegg et al. [12]. A basalt and an iron target were placed inside a sample chamber filled with 930 Pa of CO_2 to simulate the Mars atmosphere. The plasma light was collected at normal incidence and nearly coincident with the in-going laser beam using a Questar Field Model telescope with an 89 mm aperture. The telescope's Schmidt window was replaced with a fused silica window so that UV light down to ~220 nm was also transmitted. A Spiricon Scor-20 camera, typically used to measure laser beam diameters,

Table 1
Conditions for ChemCam experiments reported here.

#	Test	Distance (m)	Laser current[a]	# of Stds.	Short description
1	Thermal, distance calibration	1.6, 3, 5, 7	95 A	18	Standards in 930 Pa CO_2. Fifty spectra, 4 analysis points each.
2	Thermal, laser energy calibration	3.0	95, 80, 60 A	10	Standards in 930 Pa CO_2. Fifty spectra, 4 analysis points each.
3	Thermal, depth profile	3.0, 7.0	95 A	2	Standards in 930 Pa air. Five hundred or one thousand shots, each point.
4	Thermal, long distance	8.7	95 A	2	Iron pyrite and titanium in air. Comparison of multiple collects and single exposure of multiple laser shots.
5	Thermal, warm	3.0	95 A	6	Standards in 930 Pa CO_2
6	Calibration, large grp stds	3.0	95 A	69	Standards in 930 Pa CO_2. Forty spectra, 4 analysis points each.
7	Distance calibration	1.8–5.3, 0.5 m intervals	95 A	2	Standards in air. Fifty spectra, 1 point each.
8	Laser energy calibration	3.0	40, 50, 60, 80, 95 A	2	Standards in air. Fifty spectra, 1 point each.
9	Dust removal	3.5	95 A	1	Inclined slab with >1 mm dust, 930 Pa CO_2
10	Dust removal	2.9	60, 95 A	1	Surface normal to beam, microns of dust, 930 Pa air
11	Loose soil	2.9	95 A	1	50 and 100 shots in deep powder, 930 Pa air
12	Shot stats	2.6	95 A	1	Si wafer in air; to determine multi-shot statistics

[a] Amplifier diode current controls laser energy; 95 A corresponds to 14 mJ on target at 0 °C and ~10 mJ at room temperature; see text.

Table 2
Standards used in experiments listed in Table 1.

Name	Geologic name	Reference/source	Test
AGV2	Andesite	USGS	1,2,5,6
BCR2	Basalt	USGS	6
BEN	Basalt (foidite)	GIT-IWG	1,2,5,6
BHVO2	Basalt	USGS	1,6
BIR1	Basalt	USGS	1,6
BK2	Trachyandesite	U. Mass. (M. Rhodes)	1,6
BT2	Trachybasalt	Collected by P. King, UNM	1,6
BWQC1	Basalt	U. Mass. (M. Rhodes)	6
CADILLAC	Rhyolite	U. Mass. (M. Rhodes)	6
DH4912	Olivine	Brammer	6
GBW07104	Andesite	Brammer/NRCCRM	6
GBW07105	Basalt	Brammer/NRCCRM	1,6,9
GBW07108	Limestone	Brammer/NRCCRM	6
GBW07110	Andesite	Brammer/NRCCRM	6
GBW07113	Rhyolite	Brammer/NRCCRM	6
GBW07313	Deep-sea sediment	NRCCRM	6
GBW07316	Deep-sea sediment	NRCCRM	6
Granodike	Trachybasalt	U. Mass. (M. Rhodes)	6
GSR2	Andesite (hornblende)	NRCCRM	6
GUWGNA	Granite (greisen)	Brammer	6
GYPA	Gypsum	Brammer	6
GYPB	Gypsum	Brammer	6
GYPC	Gypsum	Brammer	6
GYPD	Gypsum	Brammer	6
JA1	Andesite	Brammer	6,7,8
JA2	Andesite	Brammer	1,2,5,6
JA3	Andesite	Brammer	1,2,5,6
JB2	Basalt	Brammer/GSJ	1,2,5,6
JB3	Basalt	Brammer/GSJ	1,2,5,6
JDO1	Dolomite	Brammer	1,2,6,9,10,11
JR1	Rhyolite/obsidian	Brammer	6
KGA-MED-S	Kaolinite + gypsum + basalt	Vaniman et al. [22]	1,2,6
M6-HAGGERTY	Basalt (kimberlite)	S.E. Haggerty collection, FIU	6
Macusanite	Volcanic glass	Fabre et al. [21]	6
MHC1356	Jarosite	MHC (Dyar et al. [14])	6
MHC2319	Melanterite	MHC (Dyar et al. [14])	6
MHC3828	Gypsum	MHC (Dyar et al. [14])	6
MO12	Basalt (andesitic)	Brammer	6
MO14	Basalt (olivine)	Brammer/RAS	6
MO7	Gabbro (orthoclase/foidite)	Brammer/RAS	6
MOPPIN	Basalt (amphibolite)	U. Mass. (M. Rhodes)	6
MSHA	Dacite/andesite	U. Mass. (M. Rhodes)	6
NAU2	Nontronite (smectite)	Vaniman et al. [22]	6
NAU2-HI-S	Nontronite + gypsum + basalt	Vaniman et al. [22]	1,6
NAU2-LO-S	Nontronite + gypsum + basalt	Vaniman et al. [22]	1,6
NAU2-MED-S	Nontronite + gypsum + basalt	Vaniman et al. [22]	1,6
Norite	Basalt	Fabre et al. [21]	6
Picrite	Basalt	Fabre et al. [21]	6
SARM51	Stream sediment + quartz	Brammer/MINTEK	6
SGR1	Sediments (kerogen, carbonate)	Brammer	1,2,6
Shergottite	Basalt	Fabre et al. [21]	6
SRM688	Basalt	NBS/NIST	6
SRM88B	Limestone (dolomitic)	NBS/NIST	6
SRM97A	Kaolinite	NBS/NIST	6
SRM98A	Kaolinite + quartz	NBS/NIST	6
STSD1	Stream sediment	Brammer	1,6
STSD3	Stream sediment	Brammer	6
STSD4	Stream sediment	Brammer	6
SWY1	Na-montmorillonite (smectite)	CMS	6
Trond	Dacite (trondjhemite)	U. Mass. (M. Rhodes)	6
Ultramafic	Basalt	U. Mass. (M. Rhodes)	6
UMPH	Syenite	U. Mass. (M. Rhodes)	6
UNSAK	Aragonite	Brammer	6
UNSZK	Feldspar	Brammer	6
VH1	Rhyolite	U. Mass. (M. Rhodes)	6
VH49	Basalt	U. Mass. (M. Rhodes)	6
VZO106	Ferrinatrite	MHC (Dyar et al. [14])	6
VZO114	Metavoltine	MHC (Dyar et al. [14])	6
WM	Gabbro	U. Mass. (M. Rhodes)	6,7,8
Ti	Ti alloy	LANL	1,2,4,5,6,7,8
Graphite	Graphite rod	LANL	1,2
Pyrite	Large pyrite crystal	D. Vaniman, LANL	4

was used to image the plasma through the Questar telescope. A filter was installed to remove any reflected laser light so that only the plasma light was seen.

2.2. Description of standards

Many natural rock samples are heterogeneous at the scale of the LIBS beam (350–550 μm diameter at distances from 2–7 m; [2]) due to variations in modal mineralogy, mineral composition, and grain size. Standards in the training model used to determine elemental abundances via PLS must be homogeneous at the beam scale size so that the certified composition corresponds to that observed by LIBS; because of this requirement, these standards were either pressed powders, glasses, or ceramics.

Table 2 presents the designations, geologic descriptions, and reference sources for each of the standards used in the experiments in Table 1. (Many of these standards are designated with slight variations in the literature. Here we use essentially all capitals and have removed most of the dashes). Most of the standards were obtained from Brammer Standard Company, Inc., which distributes standards developed by various standards institutes in countries around the world. Most of these have undergone multiple analyses for confirmation. The accepted compositions of all the Brammer standards were either taken from the certified data accompanying the standards or from Govindaraju [18] and Jochum et al. [19] (see also [20]). The compositions were verified with the original publications when available. Other standards included sulfate-bearing rocks obtained from M.D. Dyar at Mount Holyoke College and a variety of igneous rocks from the collections of J. Michael Rhodes at the University of Massachusetts. Chemical analysis protocols used for these sulfate and igneous samples are the same as those described in Dyar et al. [14] and Tucker et al. [13], respectively. As described further below, some of the standards for which a sulfate description is given, such as ferrinatrite, metavoltine, jarosite, and melanterite, consist of only small amounts of those minerals in larger fractions of accessory phases. In addition to standards from Brammer, Dyar, and Rhodes, some of the standards are splits of materials sent up on the onboard ChemCam calibration target assembly (hereafter CCCT [21,22]). Table 3 presents the accepted major oxide abundances along with selected minor and trace elements that might be detected by LIBS. Abundances of additional minor and trace elements in these standards are given in Table S1 in the supporting online material. The totals given at the right side of Table 3 include contributions from all measured elements, not just the ones shown in Table 3.

Sample grain sizes were generally less than 20–60 μm. Statistics were not available on the grain sizes of all standards. However, certification papers provided by Brammer report that plagioclase feldspar standard UNSZK has a particle size distribution by mass of 1.7%>90 μm, 1.9% between 90 and 71 μm, 2% between 71 and 63 μm, and the remainder (94.5%)<63 μm; greisen standard GUWGNA contains 4.3% between 90 and 63 μm, 30.8% between 63 and 20 μm, 29% is between 20 and 6.3 μm, and the rest (35.9%)<6.3 μm; aragonite standard UNSAK had 2.6%>90 μm, 2.1% between 90 and 71 μm, 3.8% between 71 and 40 μm, and the rest (91.5%)<40 μm; and sediment sample SARM51 had 97%<75 μm. A separate analysis was performed at the lab of R.V. Morris showing that dolomite standard JDO1 has a particle size distribution of 1.4% between 150 and 90 μm, 10.8% between 90 and 45 μm, 14.4% between 45 and 20 μm, and the majority (73.3%)<20 μm. Flight protocol dictated that on-board CCCT standards could not be powders, and instead were either natural or synthetic glasses for igneous standards [21], and ceramic discs as Martian sedimentary standards [22].

Overall the standards consisted of three types: silicates, carbonates, and sulfur-rich, described in the sections below.

2.2.1. Silicate standards

The silicate standards are of three types: igneous rock standards, some with various degrees of weathering; clastic quartzofeldspathic sediments; and some silicate minerals. Igneous standards are shown on a total alkali–silica plot in Fig. 2. The standards consist of a number of basalts and andesites, along with some more silica-rich samples. At the high-silica end are a few rhyolites and a macusanite volcanic glass which is one of the on-board CCCT [21,23,24]. Along with these are several standards added to increase the range of certain trace elements. A weathered granitic (greisen) standard, GUWGNA, was added to increase the Li and Rb range but additionally its F content is very high (2280, 2020 and 33,200 ppm, respectively; Table S1, supporting online material). A feldspar standard, UNSZK, was also added for its relatively high Li (279 ppm) and total alkali contents (4.5% Na_2O, 4.06% K_2O). Gabbro MO7 was added as a slightly sulfur-enriched (0.18% S) igneous sample. Several standards were added to increase the number of iron-rich compositions, given the iron-rich nature of Mars samples measured to date, e.g., FeO typically ≥15% (e.g., [25]). However, these turned out to be rather unusual terrestrial materials. WM is a gabbro from Woolen Mill, near Elizabethtown, New York, USA [26]. It is a clinopyroxene–garnet–oligoclase granulite with opaque oxides, apatite, and minor K feldspar and quartz. This standard has abundant magnetite and ilmenite, reflected in its high Fe and Ti contents (20.2% Fe_2O_3T; 5.81% TiO_2), and it is rich in phosphorous (1.36% P_2O_5). This WM gabbro standard should not be confused with the gabbro standard by the same acronym from the Wellgreen Complex, Yukon Territory, Canada. Another standard that was added to increase some of the minor element representations was a kimberlite (M6 Haggerty; S. Haggerty, personal communication), which contains 2.19% P_2O_5, 978 ppm Cr, 1288 ppm Ni, and high but not (so far) LIBS-detectable abundances of lanthanides (150 ppm La, 382 ppm Ce, 212 ppm Nd; Table S1, supporting online material).

A few stream and marine silicate sediments were added, in part to provide more weathered materials and to also include some organic material. Among the stream sediments, SARM51 was added, which includes a small amount of siderite and is S-enriched (0.24% S), and high in Cr (509 ppm), Pb (5200 ppm), and Zn (2200 ppm; Table 3 and Table S1 in the supporting online material).

Notes to Table 2
Brammer: Brammer Standard Company, Inc., USA.
CMS: Clay Mineral Society, USA.
FIU: Florida International University, USA.
GIT-IWG: Groupe International de Travail-International Working Group, France.
GSJ: Geological Society of Japan.
LANL: Los Alamos National Laboratory, USA.
MHC: Mount Holyoke College, USA.
MINTEK: Council for Mineral Technology, South Africa.
NBS/NIST: National Bureau of Standards/National Institute of Standards and Technology, USA.
NRCCRM: National Research Centre for Certified Reference Materials, China.
U. Mass: University of Massachusetts, USA.
UNM: University of New Mexico, USA.
USGS: United States Geological Survey.

Table 3
Major (in wt.% oxide) and relevant minor and trace (in ppm wt.) element compositions for geological standards in Tables 1 and 2.

Name	SiO_2	TiO_2	Al_2O_3	Fe_2O_3T	MnO	MgO	CaO	Na_2O	K_2O	P_2O_5
AGV2	59.30	1.05	16.91	6.69	0.10	1.79	5.20	4.19	2.88	0.48
BCR2	54.10	2.26	13.50	13.80	0.20	3.59	7.12	3.16	1.79	0.35
BEN	38.20	2.61	10.07	12.90	0.20	13.2	13.9	3.18	1.39	1.05
BHVO2	49.90	2.73	13.50	12.30	0.17	7.23	11.4	2.22	0.52	0.27
BIR1	47.70	0.97	15.40	11.33	0.18	9.70	13.4	1.81	0.03	0.03
BK2	58.83	1.94	14.77	8.78	0.19	2.82	4.64	3.35	3.99	0.71
BT2	48.57	1.52	16.46	11.09	0.15	6.42	7.92	4.48	1.28	0.44
BWQC1	52.82	1.76	12.07	17.41	0.26	3.22	6.72	4.17	0.93	0.20
CADILLAC	72.20	0.32	13.07	3.57	0.10	0.21	0.96	4.91	3.95	0.05
DH4912	41.60	0.002	0.43	7.25	0.07	49.2	0.08		0.01	
GBW07104	60.62	0.52	16.17	4.90	0.08	1.72	5.20	3.86	1.89	0.24
GBW07105	44.64	2.37	13.83	13.40	0.17	7.77	8.81	3.38	2.32	0.95
GBW07108	15.60	0.33	5.03	2.52	0.06	5.19	35.7	0.08	0.78	0.05
GBW07110	63.06	0.80	16.10	4.72	0.09	0.84	2.47	3.06	5.17	0.36
GBW07113	72.78	0.30	12.96	3.21	0.14	0.16	0.59	2.57	5.43	0.05
GBW07313	53.86	0.67	13.75	6.58	0.43	3.38	1.71	4.81	2.95	0.45
GBW07316	31.60	0.39	7.70	4.07	0.40	2.04	22.6	3.76	1.61	0.33
Granodike	48.08	3.58	12.93	15.56	0.25	6.21	6.93	4.51	0.93	0.41
GSR2	60.62	0.52	16.17	4.90	0.08	1.72	5.20	3.86	1.89	0.24
GUWGNA	71.47	0.02	14.70	5.92	0.17	0.03	0.62	0.08	2.63	
GYPA	0.45		0.10	0.05	0.00	0.18	32.9	0.01	0.02	0.01
GYPB	1.05	0.01	0.17	0.07	0.001	1.80	32.8	0.02	0.05	0.01
GYPC	3.50	0.04	0.79	0.40	0.01	5.35	30.4	0.02	0.36	0.02
GYPD	8.70	0.08	2.03	1.08	0.03	1.73	28.2	0.07	0.54	0.03
JA1	63.97	0.85	15.22	7.01	0.16	1.57	5.70	3.84	0.76	0.17
JA2	56.42	0.66	15.41	6.26	0.11	7.60	6.29	3.11	1.80	0.15
JA3	62.26	0.68	15.57	6.59	0.11	3.65	6.28	3.17	1.41	0.11
JB2	53.20	1.19	14.64	14.34	0.20	4.66	9.89	2.03	0.42	0.10
JB3	51.04	1.45	16.89	11.88	0.16	5.20	9.86	2.82	0.78	0.29
JDO1	0.20	0.001	0.01	0.10	0.01	18.4	34.1	0.01	0.002	0.03
JR1	75.41	0.10	12.89	0.89	0.10	0.09	0.63	4.10	4.41	0.02
KGA-MED-S	35.64	1.47	23.71	3.18	0.05	1.68	11.5	0.72	0.26	0.10
M6-HAGGERTY	41.37	5.90	2.75	10.65	0.20	31.2	3.01	0.29	1.35	2.19
Macusanite	73.75	0.04	16.35	0.58	0.06	0.01	0.24	4.07	3.99	0.46
MHC1356	52.66	0.08	0.55	40.28	0.01	0.10	0.20	0.02	0.60	0.17
MHC2319	68.84	0.01	0.87	17.71	0.01	0.01	0.08	0.01	0.04	0.41
MHC3828	9.44	0.11	2.25	0.44		2.67	27.4	0.12	0.93	0.04
MO12	49.87	1.61	16.74	10.54	0.14	7.38	8.73	3.85	1.12	0.45
MO14	46.85	1.62	17.06	10.85	0.15	8.05	9.60	3	0.46	0.37
MO7	40.79	3.39	17.60	12.35	0.15	6.46	14.6	2.05	0.75	1.08
MOPPIN	50.78	1.67	15.63	14.61	0.36	4.82	8.30	2.41	0.39	0.53
MSHA	63.94	0.59	17.46	4.70	0.08	1.97	5.03	4.78	1.32	0.14
NAU2	48.70	0.60	4.53	31.76	0.02	0.77	1.96	0.70	0.08	0.21
NAU2-HI-S	30.90	0.39	3.69	17.51	0.03	1.14	16.3	0.67	0.16	0.06
NAU2-LO-S	43.78	0.78	7.63	20.32	0.07	2.97	8.26	1.44	0.40	0.14
NAU2-MED-S	37.48	0.57	5.72	18.95	0.05	2.05	12.3	1.11	0.29	0.10
Norite	47.88	0.70	14.66	17.44	0.001	9.62	12.8	1.53	0.06	0.01
Picrite	43.59	0.44	12.39	22.77	0.003	11.2	8.95	3.07	0.10	0.01
SARM51	33.81	0.82	11.87	18.36	0.21	0.92	0.86	0.07	0.33	0.21
SGR1	28.24	0.26	6.52	3.03	0.03	4.44	8.38	2.99	1.66	0.33
Shergottite	48.42	0.43	10.83	19.40	0.00	6.39	14.3	1.57	0.11	0.01
SRM688	48.35	1.17	17.35	10.34	0.17	8.46	12.2	2.16	0.19	0.13
SRM88B	1.13	0.02	0.34	0.28	0.02	21.0	30.0	0.03	0.10	0.004
SRM97A	43.67	1.90	38.79	0.45		0.15	0.11	0.04	0.50	0.36
SRM98A	48.94	1.61	33.19	1.34		0.42	0.31	0.08	1.04	0.11
STSD1	42.50	0.75	9	6.50	0.50	2.21	3.60	1.75	1.25	0.38
STSD3	48.60	0.70	10.90	6.20	0.30	2.20	3.30	1.50	1.80	0.40
STSD4	58.90	0.80	12.10	5.70	0.20	2.10	4	2.70	1.60	0.20
SWY1	62.90	0.09	19.60	3.71	0.01	3.05	1.68	1.53	0.53	0.05
Trond	70.87	0.26	17.03	1.37	0.02	0.47	2.99	5.91	1.24	0.05
Ultramafic	45.75	0.27	4.04	11.94	0.20	29.2	6.12	0.85	1.06	0.14
UMPH	62.19	0.91	17.77	4.06	0.08	0.97	1.88	5.51	6.41	0.26
UNSAK	0.64		0.11	0.13		0.11	54.9	0.05	0.04	0.03
UNSZK	74.38	0.04	14.19	1.75	0.03	0.07	0.43	4.50	4.06	
VH1	73.61	0.34	13.68	2.01	0.04	0.36	1.13	3.40	5.60	0.07
VH49	47.50	0.82	17.83	9.02	0.15	11.0	10.8	2.55	0.18	0.09
VZO106	69.08	0.49	0.57	7.39	0.01	0.02	0.42	2.72	0.73	0.03
VZO114	43.65	0.27	3.67	0.19	0.00	0.05	16.2	0.71	0.22	
WM	43.29	5.81	12.04	20.24	0.26	4.44	9.01	2.32	0.45	1.36

[a] Totals include additional trace elements given in the supporting online material.

2.2.2. Carbon-rich standards

Because ChemCam can observe carbon emission peaks, and as carbon is an important element for the goals of the MSL mission, and also considering that APXS cannot detect carbon directly, it was important to analyze standards that contain C. The carbonate standards were selected mostly out of convenience and consist of six limestone and

Table 3 (*continued*)

SO_3T	H_2O+	CO_2	As	B	Ba	Cu	Li	Sr	Zn	Total[a]
					1130	53	11	661	86	98.97
0.04					677	21	9	340	127	100.26
0.07	2.24	0.74	2		1025	72	13	1370	120	100.40
	0.20				131	127	5	396	103	100.75
			0	0	7	119	3	109	72	100.71
	1.38				1001			487	210	101.72
					480	50		559	28	98.53
	3.26				122			161	133	102.96
	0.69				711			49	106	100.23
		0.05								99.24
0.05	1.50	3.47	2	5	1020	55	18	790	71	100.58
0.02	2.86	0.19	1	4	498	49	10	1100	150	101.23
0.09	2.12	32.40	5	16	120	23	20	913	52	100.21
0.06	1.79	1.03	6	11	1053	9	18	318	164	99.99
0.02	1.18	0.52	1	4	506	11	13	43	86	100.24
	5.50		6	125	4400	424	60	267	160	98.93
	4	17.30	5	84	2500	231	35	667	142	99.94
					212			264	58	99.56
0.05	1.54	3.46	2	5	1020	55	18	790	71	100.61
			7		51		2276		78	99.65
46.20	19.40	0.47	0		28			930	5	99.99
41	17.80	5	0		22			118	5	99.81
33	14.37	11.20	3		53	10		296	17	99.55
36.70	16.39	3.60	3		107			152	18	99.25
0.01	0.72		3	24	303	41	10	264	91	100.14
	1.12		1	23	315	28	29	250	65	99.16
	0.20		5	25	318	45	14	294	68	100.27
0.005	0.25		3	30	208	227	8	178	110	101.18
0.002	0.18		2	15	251	198	7	395	106	100.85
0.02	0.40	46.50	0	1	6	1.41	0.4	119	34	99.87
0.003	1.18		16	133	40	1.40	62	30	30	100.11
13.40			3	23,107	140	30	7433	152	50	94.89
					1909			1282	77	99.76
				1573	1.30	2.40	3528	1.30	109	100.13
	3.03		1		294	15		51	7	97.79
36.18			965		455	284		1931	58	124.92
35.61	15		1		79	7		2053	59	94.48
0.01	0.18			9.30	311	54	9	865	130	101.04
0.01	1.73			8.70	172	66	8	468	108	100.06
0.45	0.70	0.03		4.50	7480	59	5	1745	65	101.81
	2.32				273			405	153	102.05
	0.99				367			483	51	101.18
	11.69				46			134	130	101.02
21.07			1	23,107	56	10	7433	144	60	95.05
5.33			1	23,107	162	30	7433	236	90	94.39
13.54			1	23,107	107	20	7433	185	70	95.32
				11	355	6	44	284	9	104.76
				12	1283		7	1481		103.17
0.60			97		335	268		44	2200	69.29
3.82		39.58	67	54	290	66	147	420	74	99.71
				9	1158	43	8	654	7	101.77
			2	1	200	96		169	58	100.69
		46.67						64		99.57
	13.32				670		510	1500		99.77
	12.44		11		270		325	330		99.63
0.45		45.07	23	89	630	36	11	170	178	114.31
0.35		30.78	28	82	1490	39	23	230	204	107.46
0.22		15.02	15	46	2000	65	14	350	107	103.97
0.12		1.33								94.71
	1.11				347			668	32	101.51
	7.45				434			283	90	107.50
	0.63				2980			382	77	101.20
0.11		43						2800		99.88
			5			12	279		19	99.49
	0.45				277			50	27	100.80
	1.53				37			234	57	101.61
12.46	6.02		27		482	643		120	2012	101.09
23.62	11.22		24		63	13		160	5	99.90
					351			400	272	99.46

dolomitic limestone standards, one containing aragonite (UNSAK), which was added to increase the represented range of Sr (2800 ppm in this standard). There were several other standards with appreciable carbon: SGR-1, which is a very organic-rich shale containing 28% total C (24.8% organic carbon); stream sediment STSD-1, containing 12.8% C (apparently all organic, as X-ray diffraction at LANL indicated no

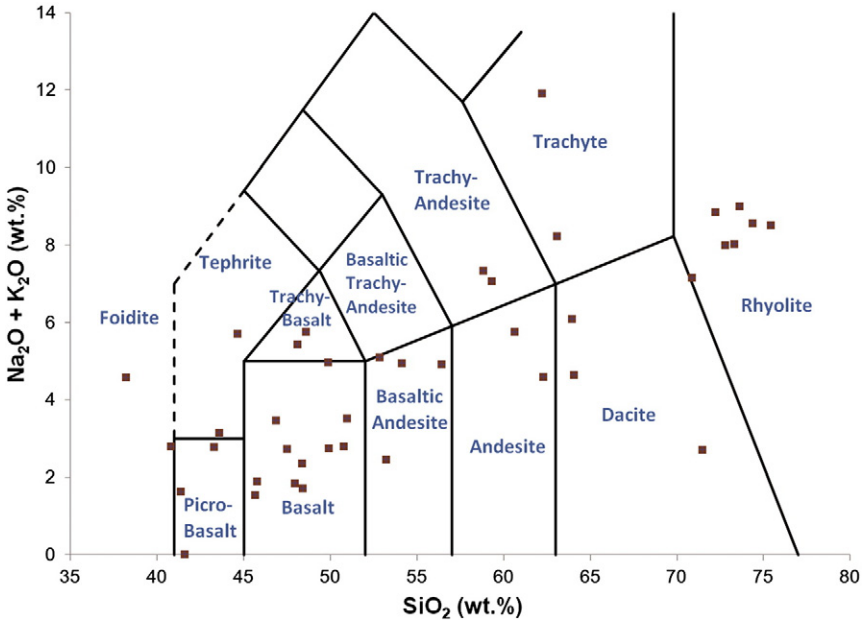

Fig. 2. Total alkali–silica plot of the igneous standards used in the large group calibration performed at 3 m (#6 in Table 1).

carbon-bearing minerals), deep-sea sediments GBW07316 and 07315 with 17.3% and 3.6% CO_2, respectively; gypsum standard MHC2319 with 1.5% C, stream sediments GBW07305 and 07306 with 3.6 and 2.0% CO_2, respectively; hornblende andesite standard GSR-2 with 3.5% CO_2; and andesite GBW07104 with 3.47% CO_2. In these samples the C may be present either as carbonate phases or as organic carbon. Carbon-bearing minerals most likely to be found by MSL, such as siderite, thought to comprise a significant fraction of the Comanche rock analyzed by the Spirit MER rover [27], were not among the carbonate standards used. In general, samples with high iron content result in poorer carbon detection limits due to emission line interferences. No nitrate, carbide, or nitride standards were analyzed prior to launch; however, the CCCTs include a graphite disk, in part to ensure the identification of carbon emission lines on Mars.

2.2.3. Sulfur-rich standards

Gypsum is the only sulfur mineral to be represented in relatively pure form (GYPA). Several other gypsum samples with varying degrees of purity were analyzed (GYPB, GYPC, GYPD, MHC3828). The remaining sulfur-rich standards represent relatively impure mixtures consisting of the host rock with coatings of jarosite (MHC1356; 52.7% SiO_2), ferrinatrite (VZO106; 69.1% SiO_2), metavoltine (VZO114; 43.7% SiO_2), and melanterite (MHC2319; 68.8% SiO_2). These standards were not analyzed by X-ray diffraction (XRD), so the accessory minerals are not known. In addition to these standards, four anhydrite-bearing ceramic discs have been synthesized and mounted as standards on Curiosity. Sulfur content in these standards ranges from 2.1 to 8.4 wt.%. A detailed description of these standards is in Vaniman et al. [22].

2.2.4. XRD characterization of selected standards

Mineral identifications and abundances for several samples (igneous standards AGV2, BCR2, BEN) are reported by Campbell et al. [28]; other information on mineralogy of samples is provided by Brammer (igneous standards GUWGNA, VS MO7), by UNS (aragonite UNSAK), and for the Canadian gypsum-rich standards GYPA, GYPB, GYPC, and GYPD by Domtar, Inc. Because mineralogy may play a part in eventual fundamental treatments of plasma generation and spectral analysis, several other standards that lacked mineralogical information were selected for XRD analysis at Los Alamos National Laboratory (LANL). The XRD analyses were performed using a Siemens D500 diffractometer with a monochrometer and Cu Kα radiation. All samples were analyzed at 2–70° 2θ at steps of 0.02° with 12 s counting time per step. Diffraction patterns were analyzed using JADE software. Results are listed in Table 4 along with the mineral abundances reported from other sources. The standards are listed in alphabetical order but they can be considered as representative of several lithologic or mineralogic types, as described below.

2.2.4.1. Stream sediments. Stream sediment geostandards analyzed were SARM51, STSD1, STSD3, and STSD4. SARM51 contains significant amounts of smectite and kaolinite, but the STSD samples have no detectable smectite or kaolinite. The STSD stream sediments contain significant amounts of mica, chlorite, and amphibole that are not found in SARM51.

2.2.4.2. Marine sediments. Marine sediment geostandards analyzed were GBW07313 and GBW07316. These sediments contain poorly crystalline smectite (or illite/smectite) and halite. Quartz abundance is lower (<20%) than in the stream sediments; the sample lowest in quartz contains kaolinite as well as smectite. GBW07314 contains no calcite, while the calcite content of GBW07316 is 53%; this calcite-rich sample lacks feldspar. In GBW07313 the feldspar is best fit as sodic to intermediate plagioclase. Chlorite observed in GBW07313 could alternatively be glauconite.

2.2.4.3. Carbonate sediments, aragonite, and gypsiferous samples. A range of carbonate sediments and gypsiferous samples are in the standard suite, including dolomite (SRM88B, JDO1) and dolomitic limestone (GBW07108), and the Canadian Certified Reference Materials (CCRM) gypsiferous samples GYPA, GYPB, GYPC, and GYPD. Dolomite SRM88B is essentially pure dolomite whereas dolomite JDO1 contains about 7% calcite. The dolomitic limestone GBW07108 is mostly calcite (54%) with lesser dolomite (23%) plus quartz, mica, and kaolinite. The aragonite sample UNSAK is a mixture of sub-equal amounts of calcite and aragonite. The CCRM gypsiferous samples range from almost pure gypsum (GYPA, 97.4%) to more complex mixtures (GYPC has only 70.4% gypsum). Diluent phases in these samples include quartz, feldspar, dolomite, calcite, anhydrite, mica, and kaolinite. The mineral components in the gypsiferous samples were determined by Domitar, Inc. using XRD and thermal analyses along with phase separation and concentration. The higher precision of these combined methods is reflected in the accuracies reported in Table 4.

2.2.4.4. Igneous rocks and olivine. Relatively unaltered igneous standards range from basalt (BCR-2) or gabbro (VSMO7) to andesite (AGV2) and granite (GUWGNA). GUWGNA is fluorine rich, containing topaz and fluorite. A zeolitized benmorite (BEN) is also in the standard suite, as is a chloritized olivine (DH4912).

2.2.4.5. Clay minerals. Clay minerals, or materials rich in clay minerals, include Clay Minerals Society (CMS) source clays NAU2 and SWY1 as well as kaolinite-rich geochemical reference materials SRM97A and SRM98A. It should be noted that the CMS source clays are mineralogical reference materials and are not accepted geochemical standards; the analyses listed here are published results of representative splits but do not represent precise analysis of the splits used with our LIBS experiments. These data are for comparison only. The SRM kaolinites are accepted geochemical reference materials but are not pure kaolinite; SRM98A in particular is only 40% kaolinite, the rest being mica, quartz, and anatase. SRM97A also contains anatase.

2.2.4.6. Kerogen-rich sediment. Standard SGR1 is an organic-rich material with a kerogen component containing a significant amount of kerogen. Kerogen is X-ray amorphous and was not quantified by XRD. The mineral abundances of quartz, feldspar, dolomite, calcite, and mica reported in Table 4 are corrected from the values determined by XRD assuming ~30% kerogen content. The estimate of kerogen content is based on 24.8% total organic carbon reported in the USGS certificate of analysis, allowing that ~80% of the kerogen is organic carbon.

2.3. Data treatment

The information of interest in LIBS data is principally contained in the emission lines. Processing of ChemCam data is done in two general steps. The first step, to achieve Level 1 products, is shown in the middle boxes in Fig. 1, and consists of removing the non-laser-induced background ("Dark Subtract"), de-noising the spectrum, removing the electron continuum, and calibrating for wavelength and instrument response for a sample at a given distance. The result is emission peak spectra in units of photons emitted per pulse in radiance units (photons/pulse/mm^2/sr/nm). Processing of data to Level 1 is also called pre-processing. Level 2 processing involves using multivariate training models based on spectral libraries to obtain elemental abundances and to classify the sample relative to other spectra. Particularly for minor or trace elements Level 2 processing involves univariate analyses of the strongest and most stable emission peaks of the given element. This section describes each of the preprocessing (Level 1) steps in detail. The Level 2 processing and results are presented later in the paper. For the Level 1 processing an example spectrum is shown with its component contributions in the VNIR range in Fig. 3. This particular spectrum was selected to illustrate the effectiveness of the processing in the worst case in terms of signal to noise. It is the spectrum of a basalt (BIR1) observed at a relatively long distance (7 m), hence its signal is relatively low.

2.3.1. Non-laser dark subtraction and de-noise

A non-laser "dark" spectrum is taken in close temporal proximity to the LIBS spectra. During pre-delivery calibrations a dark spectrum was taken for every two samples analyzed. The dark spectrum typically consists of fifty collects using the same spectrometer settings as the active, but without the laser pulses. With no need to wait for the laser, the dark spectra are taken in rapid succession. The dark subtraction routine finds the non-laser data file nearest in time to the active spectrum of interest and obtains the difference. Prior to subtraction, the routine performs a 'leveling', which uses the means of the 50 non-exposed pixels on either side of the active ones to adjust the non-laser dark spectrum to the appropriate level to subtract from the active spectrum. The leveling is needed when the CCDs are <-10 °C, because the longer operation time of taking spectra warms the CCDs and induces higher noise levels than in the dark spectra which are taken as rapidly as possible. In all cases the dark spectra are averaged before subtraction. The dark subtraction also removes an offset of 300–500 DNs that is added in the analog-to-digital conversion of data from each spectrometer to ensure that the conversion does not produce negative values.

To remove white noise, the spectrum is expanded at different wavelet scales. Wavelet analysis involves a convolution of the signal with a kernel (the wavelet) of specific mathematical properties. These properties define an orthogonal basis, which conserves energy and guarantees the existence of an inverse to the wavelet transform [29].

The principle behind the wavelet transform is to hierarchically decompose the input signal into a series of consecutively lower resolution reference signals and their associated detail signals. At each decomposition level, L, the reference signal has a resolution reduced by a factor of 2^L with respect to the original signal. Together with its respective detail signal, each scale contains the information needed to reconstruct the original signal at the next higher resolution level. Wavelet analysis can therefore be considered as a series of bandpass filters and be viewed as the decomposition of the signal into a set of independent, spatially oriented frequency channels. Hence, a function in this decomposition can be completely characterized by the wavelet basis and the wavelet coefficients of the decomposition.

The decomposition is performed by an iterative application of a pair of quadrature mirror filters (QMF). A scaling function and a wavelet function are associated with this analysis filter bank. The continuous scaling function $\phi(x)$ satisfies the following equation:

$$\phi(x) = \sqrt{2}\sum_n h(n)\phi(2x-n) \tag{1}$$

where $h(n)$ is the low-pass QMF. The continuous wavelet $\psi(x)$ is defined in terms of the scaling function and the high-pass $g(n)$ QMF through:

$$\psi(x) = \sqrt{2}\sum_n g(n)\phi(2x-n). \tag{2}$$

In our particular application, we used a "stationary" or redundant transform, i.e., decimation is not carried out which is more appropriate when filtering of a signal is considered. In this case the wavelet coefficients are derived from the difference between two successive scaling passes. The scaling function we use is a B_3-spline and the associated QMF h is defined in terms of its Laurent polynomial as:

$$h(z) = \frac{1}{16}\left(z^{-2} + 4z^{-1} + 6z^0 + 4z^1 + z^2\right). \tag{3}$$

The algorithm we implemented for this undecimated cubic spline wavelet transform is described in [30] and the spectrum is mirrored at both edges so as to avoid the discontinuities there during the process.

At each scale, the noise standard deviation is iteratively computed, assuming a white Gaussian noise. Only the wavelet coefficients with values greater than a defined threshold, typically three times the noise standard deviation, are returned. Finally, the de-noised spectrum is obtained by summing all modified wavelet scales. The noise removed by this routine is shown in Fig. 3b for the VNIR range. For this example, the amplitudes rarely exceed one count, or digital number (DN). By comparison with the processed spectrum (Fig. 3a), the denoise algorithm tends to ignore the wavelengths corresponding to strong peaks.

2.3.2. Continuum removal

LIBS spectral emission contains a background continuum due to Bremsstrahlung and ion-electron recombination processes, which contains non-relevant spectral information. It is removed from each spectrum applying the following procedure: similar to the de-noise algorithm, the spectrum is decomposed into a set of cubic spline

Table 4
Measured mineral compositions, in percent.

Name	Description	Smectite	Kaolinite	Mica	Chlorite	Amphibole	Quartz	Feldspar	Olivine	Calcite	Aragonite	Dolomite	Halite	Clinopyroxene	Gypsum	Anhydrite	Source
AGV2	Andesite						11	77						12			1
BCR2	Basalt							69						31			1
BEN[a]	Altered basalt			1					12					49			1
DH 4912[b]	Altered olivine		<1		14	<1			85								2
GBW 07108	Limestone		4	6			12			54		23					2
GBW 07313	Marine sediment	~6		20	22		20	22					10				2
GBW 07316	Marine sediment	~5	10	16			9			53			7				2
GUWGNA[c]	Granite		5	38			50										3
GYPA	Gypsum						0.4					0.2			97.4	2	4
GYPB	Gypsiferous						0.5			2.4		8			87.1	2	4
GYPC[d]	Gypsiferous						1.6	1.5				25			70.4	1.5	4
GYPD[d]	Gypsiferous		<1	<1			8	2				9			81		4
JDO1	Dolomite									7		93					2
MO7[e]	Gabbro			11				33	8					38			3
NAU2	Nontronite	~95						~5									2
SARM 51[f]	Stream sediment	~25	35	<1			36										2
SGR1[g]	Kerogen sediment			<1			10	27		1		32					2
SRM 88B	Dolomitic limestone						0.2			0.8		99					2
SRM 97A[h]	Kaolinite		94														2
SRM 98A[i]	Kaolinite-mic–quartz		40	25			25										2
STSD1[j]	Stream sediment			6	14	14	34	32									2
STSD3	Stream sediment			6	17	5	31	41									2
STSD4	Stream sediment			2	6	6	41	45									2
SWY1	Na-montmorillonite	~90					~3	~6		<1							2
UNSAK	Aragonite									54	45						5

Data sources: 1 = Campbell et al. [28], 2 = LANL X-ray diffraction measurement, 3 = Brammer certificate, 4 = Domtar certificate, 5 = UNS certificate.

[a] BE-N also has 6% magnetite, 2% apatite, 11% zeolite (gonnardite), and 19% nepheline.
[b] DH 4912: minor talc may be present.
[c] GUW GNA also has 1% fluorite and 5% topaz.
[d] Feldspar in GYP-C and GYP-D is reported as microcline.
[e] MO7 (Brammer VS MO7) also has 2% periclase.
[f] SARM 51 also has 4% siderite.
[g] SGR-1 also has 24.8% total organic carbon (~30% kerogen).
[h] SRM-97A also has 6% anatase.
[i] SRM-98A also has 10% anatase.
[j] STSD-1 also has 1% zeolite.

undecimated wavelet scales. In this space the local minima or convex hulls are found. The search for these minima starts from the larger scales and proceeds to the smallest. It is stopped at a scale which is fixed by the user. At the end, a spline function is interpolated through the different minima. The default parameters are six (value of L) for the UV and VIO spectral ranges, and five for the VNIR. Increasing this parameter produces a smoother continuum; on the other hand, a lower number gives a continuum that follows the spectrum more closely. This procedure does not fit the VNIR range well in the region where the instrument transmission has a large drop between 850 and 905 nm [1]. To improve this region, the continuum removal is re-done over the VNIR pixel range from channels 1801 to 2048 using a parameter value of three.

The continuum that is removed by this procedure is shown in Fig. 3c for the VNIR portion of the spectrum. This is the spectral range which has by far the strongest relative contribution of the continuum. It is amplified in this spectral range relative to the other two ChemCam spectral ranges, as the VNIR resolution is between four and five times poorer than the UV and VIO ranges. Because the emission peaks are spectrally narrow, their per-channel amplitudes are not reduced by increased pixel resolution in the UV and VIO; however, the per-channel continuum contribution decreases. The continuum contribution shown in Fig. 3c has an irregular shape because it is not corrected for the instrument optical response. Various spectra have been examined with the continuum removal either before or after correcting for instrument response, and the removal works slightly better when performed prior to instrument response correction. Looking at Fig. 3a, one can see that the continuum removal was not perfect in this case, leaving perhaps one to two DNs, or approximately 10% of the original continuum in some areas. This is true near the sodium line at 589 nm, where the instrument response contains a feature from one of the spectrometer's dielectric mirrors [1]. Other areas exist where the continuum was not perfectly removed, including at wavelengths longer than 860 nm. As shown in Fig. 3c, continuum was actually added rather than subtracted in this region due to the difficulty of fitting a very large absorption feature in the optical system in this range [1]. For this reason, Level 2 LIBS processing masks the region beyond 849 nm.

2.3.3. Wavelength calibration

We start with a baseline calibration for each spectrometer, produced from a LIBS spectrum taken during the rover system thermal testing on March 22, 2011 using as a target a Ti plate at 2.8 m distance and at approximately Mars atmospheric pressure. This spectrum was selected because it was obtained late in the rover testing period, and therefore was assumed to be close to flight-like, and the spectrometers were at 25 °C, approximately the temperatures expected in the body of the rover during operation on Mars (a thermo-electric cooler reduces the temperatures of the CCDs, but has much less effect on the temperature of the overall spectrometer structures). The spectrum of titanium was used as our internal standard because Ti provides multiple emission peaks in all three of the spectral ranges, facilitating accurate wavelength calibration. This spectrum was used to provide a baseline channel-to-wavelength calibration. All other spectra are adjusted to match this wavelength-channel map. As Mars pressure is approximately 1% of standard terrestrial pressure, we calibrated to vacuum wavelengths [31], the difference between Mars pressure and vacuum being well within the uncertainty.

An adjustment of other spectra to this map is carried out using partial matched filters on the spectra. This is ideally done by comparing Ti spectra taken at regular intervals during pre-launch calibrations against the above-mentioned reference spectrum. The technique also works with some success matching the LIBS spectra of other materials to the Ti baseline wavelength-pixel map or another similar and well-calibrated spectrum. The partial matched-filter technique splits the given spectral ranges (2048 channels for each spectrometer) into several windows of a given channel length, l. Each single window is matched against the baseline Ti spectrum, and a channel shift giving the best correlation between the two spectral windows is defined for this window. In practice, the wavelength drift is essentially a function of spectrometer temperature. Based on thermal characterization of the ChemCam spectrometers, the maximum expected shift is about three channels for a ~20 °C operational temperature range. In some cases where the temperature varies more than expected, a higher maximum shift can be specified, and the time required for the calculations varies linearly with this value. Typically eight windows are used ($l = 256$ for 2048 channels in the spectral range), which give eight channel shift values over the spectral range. This function of eight values is then interpolated over the spectral range by a third-degree polynomial. The channel shift function is then applied to the wavelength values to match each channel to the baseline Ti wavelength-channel map. Using a single window of 2048 channels gives the average shift of the whole spectral range with the best correlation between the default and the new spectrum.

As the above procedure alters the distance in wavelength space covered by each channel, re-sampling of the intensities must be carried out to adjust the spectrum by fractions of a channel and re-plot it on the baseline channel-to-wavelength map. The re-sampling uses a spline fit to all peaks using the INTERPOL function in IDL.

2.3.4. Instrument response measurement, normalization, and distance correction

To make comparisons between different instruments and also to correct for optical response changes that take place over time on a given instrument, spectra must be corrected for optical response. The instrument response (IR) measurements and corrections are described in Wiens et al. [1]. A brief description of the IR function as applied to the ChemCam calibration and distance correction is included here. The IR function is written as:

$$\mathrm{DN} = L \times A \times \Omega \times \Delta\lambda \times \Delta t \times \sigma + O_{ff} \quad (4)$$

where DN is the digital number (intensity in counts), L is the photon spectral radiance in photons/second/cm^2/sr/μm wavelength, A is the source area imaged, in cm^2, Ω is the solid viewing angle in sr, $\Delta\lambda$ is the detector wavelength bin width in μm, Δt is the integration time in seconds, σ is the amplified conversion gain in DN/photon, and O_{ff} is the offset provided in the analog-to-digital conversion electronics [1]. In Eq. (4), L and Ω are inversely dependent upon the distance from the ChemCam telescope to the target while A is increasingly dependent on distance. ChemCam level 1 data are provided in two forms: Level 1A data are given in DN, without correction for IR or distance. Level 1B data have the IR applied and are given in photon radiance.

Data used for both classification and quantitative elemental compositions, done under Level 2 processing, are mean centered and variance normalized (MCVN) as follows. The mean intensity (m) and standard deviation (s) for each spectral range (UV, VIO, VNIR) are calculated. The MCVN intensity is calculated as:

$$I_{(\mathrm{MCVN})\lambda} = (\mathrm{DN}_\lambda - m)/s \quad (5)$$

such that the average intensity for each spectral range is 0, the minimum value is a negative number, and the standard deviation is 1.

Significant efforts were made to characterize the spectral response as a function of distance. Several observables change as the distance from the ChemCam telescope to the target changes including image source area (A), solid viewing angle (Ω), source radiance (L) as well as the laser spot size [2]. While the laser spot size increases as the distance to target increases and the laser energy remains constant, the irradiance (W/cm^2) decreases with increasing target distance. This reduction in flux with increasing distance results in a reduction in

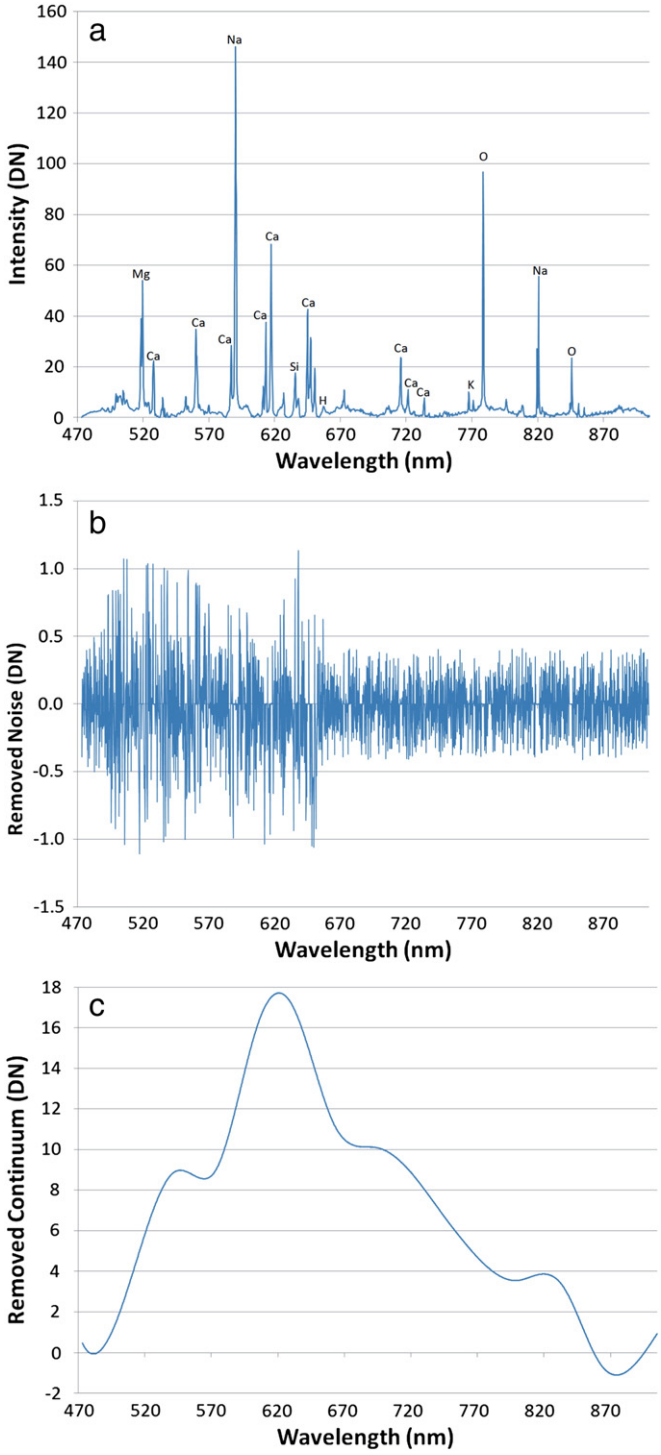

Fig. 3. Contributions of various processing steps to the total signal for the VNIR portion of the spectrum for standard BIR1 at 7 m during TVAC distance tests (#1 in Table 1). Part (a) shows the spectrum after the noise (b) and continuum (c) were removed.

the total emission intensity coming from the LIBS peaks as well as in the continuum emission. The distance dependence of the continuum emission is the primary reason for its removal, described in Section 2.3.2. above. The flux dependence on distance was expected to reduce the number of emission lines observed especially at the 7 m maximum stand-off distance. However, this was not ultimately observed in the calibration data discussed in this paper. Investigations into the distance dependence on the specific elemental lines determined that distance had little to no impact. In fact, the laser-to-sample coupling, described below, has a far greater impact on the emission line intensity variations than any distance dependence up to the maximum 7 m stand-off distance. Consequently, it was determined that applying Eqs. (4) and (5) effectively correct for the stand-off distance.

3. Results and discussion

3.1. LIBS plasma size

An important parameter for the design of ChemCam was the physical and angular sizes of the portion of the plasma containing emission lines. Generally, the plasma size is reported as a cross section observed orthogonal to the laser beam (e.g., [5]), while the geometry relevant for ChemCam is with a viewing angle coincident with the beam. Previously it was reported (e.g., [4,32]) that plasmas created under reduced-pressure environments were not only brighter but also significantly larger in diameter.

We measured the diameter of the emission line portion of the LIBS plasmas when viewed at approximately normal incidence to the target with a laser energy of 17 ± 1 mJ. An iron target was measured at two different distances under conditions nearly equivalent to ChemCam's laser on Mars. At 4 m the FWHM of the emitting portion was found to be 380 μm and the diameter at $1/e^2$ (13%) of the maximum was 565 μm ± 10% (Fig. 4) as measured by the Spiricon camera. A basalt target at this distance gave similar readings but with a narrower peak, at 270 μm FWHM and a diameter at 13% of maximum at 608 μm. At 9 m the diameter of the plasma produced on the Fe target was slightly larger than at closer distances, at 420 μm FWHM and 700 μm at $1/e^2$ of maximum. Using the Spiricon camera, the size of the emission plasma from the Fe target at 4 m distance was tracked with laser energy between 12 and 20 mJ. The FWHM increased from 330 to 430 μm and $1/e^2$ of maximum increased from 530 to 610 μm.

In addition to taking images of the total emission, a trifurcated fiber and spectrometer were also used to check the extent of the portion of the plasma providing emission lines. The fibers, each 200 μm in diameter, were positioned at the focal point of the telescope, with a target positioned in a chamber with 930 Pa of CO_2 at a distance of 6.5 m. The telescope system had an effective magnification of 4.75 so that each fiber imaged an area of 950 μm in diameter FWHM. The centers of the areas imaged by the fiber were 1.23 mm apart at the target. This arrangement was used to confirm that the emission line portion of the plasma was smaller than the image space of the different fibers. With the emission line signal on one fiber, continuum was observed in another and nothing in the third.

These results differ from earlier reports [6,32] that the emission line portion of the plasma was several mm in diameter at Mars pressure. Instead, the emission-line portion of the plasma is approximately the same size as the laser beam itself, which was measured on ChemCam using the diameter of the bare Al exposed on a black anodized Al plate, observed to range from 350 to 550 μm between 2 and 7 m [2]. The field of view of the optical fiber at the back of ChemCam's telescope is approximately 0.6 μrad FWHM [2]. If the LIBS laser and the optical fiber are perfectly aligned, the fiber should collect essentially all of the emission light within its FWHM acceptance irrespective of the distances of interest to ChemCam. Tests with ChemCam showed that the plasma signal increased strongly with decreasing distance to as close as 1.5 m, which was the closest distance tested, in agreement with the above plasma size results and with alignment tests made by backlighting the fiber [2].

3.2. Plasma temperatures

Laser-induced plasmas are complex, inhomogeneous structures that form and decay quickly, and are characterized by their temperature and electron number density (e.g., [33]). The Boltzmann equation can be used to determine the plasma temperature, with the

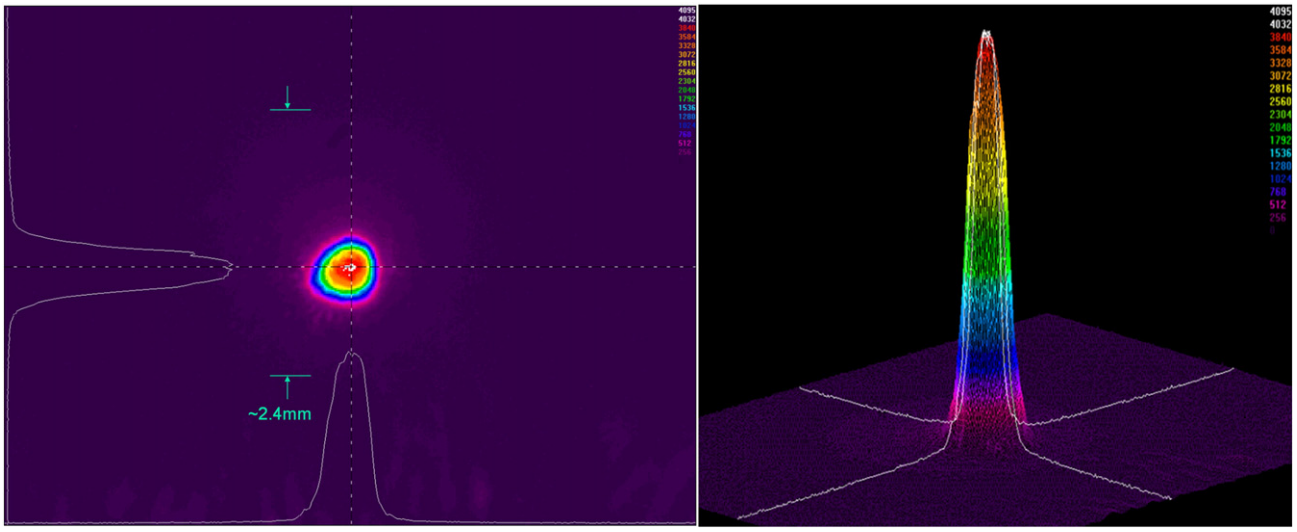

Fig. 4. Image of the visible emission from a plasma generated with a 17 mJ laboratory laser pulse incident on an iron plate in 930 Pa of CO_2 at 4 m distance, intended to determine the size distribution of the plasma.

assumptions that the plasma is in local thermodynamic equilibrium (LTE) and is optically thin [34]. To be in LTE, the electron density must be high enough for the rate of collisions in the plasma to exceed the radiative rate [34]. For a single species, the Boltzmann equation can be used to find this temperature from the slope of the linear relationship between the upper energy level of the transition E_k and $\ln(I{\cdot}\lambda/(g_k \cdot A_{ki}))$, where I is the spectrally integrated line intensity, λ is the wavelength of the transition, g_k is the upper level statistical weight and A_{ki} is the atomic transition probability [35]. The slope is equal to $-1/(kT)$, where k is the Boltzmann constant and T is the plasma excitation temperature. In this study, we sought to determine the relationship between plasma temperature with stand-off distances of 3, 5, and 7 m to understand how the stand-off distance influences plasma properties using spectra from Test #1 in Table 1.

While numerous studies have stressed the importance of LTE as a prerequisite to the calculation of plasma temperatures and recommend selecting the observational gate width to exclude the initial and final parts of the plasma, ChemCam cannot be modified in such a manner and each plasma is observed over its entire duration. Therefore it is likely that no ChemCam observation can be assumed to be in LTE. To test for LTE, Cristoforetti et al. [36] outlines three requirements for LTE in inhomogeneous and transient plasmas: (1) the electron number density exceeds a certain level at a particular temperature for a particular energy difference, referred to as the McWhirter criterion, (2) there is sufficient time for excitation and ionization equilibria to be achieved and this time is less than the variation rate of thermodynamic parameters, and lastly (3) the diffusion length of atoms and ions is less than the variation length of temperature and electron density. None of these criteria can be checked with the currently available ChemCam data set and it is assumed that the spatially and temporally averaged observations are not in LTE, and as a result, the absolute temperatures may not have physical meaning. However, the relative differences between values obtained at different distances may provide useful information.

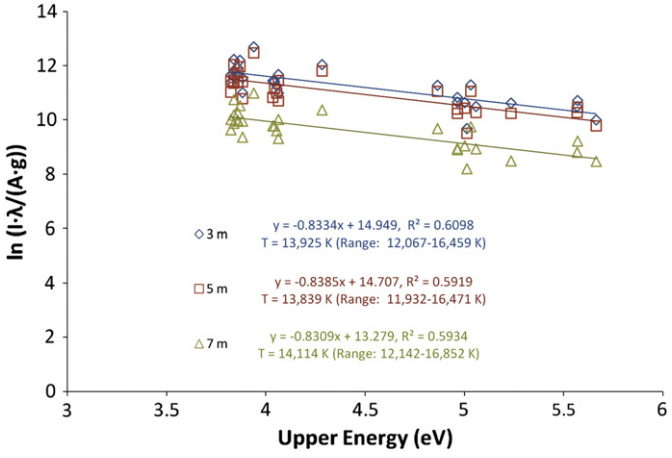

Fig. 5. Boltzmann plots of selected Ti II lines (Table S2, supporting online material) from standard BHVO2 positioned 3, 5, and 7 m from the instrument. The temperature ranges listed are based on the upper and lower bounds from the standard error of the slope. Error bars (not shown) for the y-axis are based on the standard deviation between the 3 replicate peak areas and are approximately the same size as or smaller than the data points.

Prior to the construction of ChemCam, several studies were conducted under Mars-like conditions with equipment anticipated to approximate ChemCam. Plasma temperatures in one such experiment were determined by Sallé et al. [37] using a gated echelle spectrometer. They found excitation temperatures on six rocks to be between 9000 and 11,000 K using the suite of neutral Fe lines between 350 and 400 nm at a single stand-off distance of 3 m. However, the majority of these lines are at wavelengths that fall outside the range covered by ChemCam's spectrometers, and therefore another set of lines is required. Due to the resolution of ChemCam (0.15 nm FWHM between 240 and 342 nm, 0.20 nm between 382 and 69 nm, and 0.65 nm between 474 and 906 nm) and possibly due to line broadening from the inclusion of the entire plasma emission in the final observation, finding relatively isolated lines that are present in spectra at 3, 5, and 7 m distances was difficult. Attempts were made to find a sufficient number (>10) of neutral or singly ionized lines of Fe, Ca, Mg, Ti and Si to use in the Boltzmann plot. Finally, 29 Ti II lines (Table S2, supporting online material) between 307 and 457 nm were chosen as they are resolvable and are strong enough to be observed at 7 m.

Fig. 5 shows an example of the Boltzmann plots at each distance for BHVO2, a basalt. The peak areas used are the means of the peak areas from 3 spectra that are themselves averaged from 45 individual-shot spectra. Each group of 45 spectra was selected to be distributed between the 4 analysis points on each sample pellet, thus reducing heterogeneity from either the sample or the sampling parameters. Uncertainties in the y-axis direction of the Boltzmann plot are based on the standard deviation of the 3 peak areas and are not shown as

they are the same size or smaller than the data points on the chart. The Ti II lines were not checked for self-absorption but are believed to not suffer from it due to the decreased atmospheric pressure (930 Pa) and the relatively low concentration of Ti (maximum of 2.73% TiO_2) although it is recognized that, in the absence of a low-pressure environment, self-absorption can occur at concentrations as low as 0.1% [9]. The 29 Ti II lines were typically fit with Voigt profiles, although occasionally Gaussian profiles were used and a linear background was subtracted locally over a small wavelength range. The PeakFit software from Systat Software, Inc. was used for background removal and peak fitting. To determine the suitability of each peak for inclusion in the analysis, peak ratios of adjacent peaks were found at each distance. The standard deviations between the ratios at each distance were inspected and one ratio was found to change considerably with distance and had a standard deviation exceeding 1.0 in 2 of the 3 samples. However, each peak in this ratio had low standard deviations in ratios with other nearby peaks and neither peak was overly influential in the Boltzmann plots; therefore, both peaks were kept in the final analysis.

To our knowledge no studies of plasma temperatures have been conducted at comparable stand-off distances. However, several studies have been done at various energies with distance held constant. This results in a change in on-target fluences that can be compared to the fluences seen by ChemCam which have a constant energy and a varying spot sizes (radius of ~120 μm at 3 m and 200 μm at 7 m). With the laser at −10 °C, the ChemCam laser operates at 15 mJ per pulse, resulting in on-target fluences for the given spot sizes of 34 J/cm2 at 3 m, 19 at 5 m and 12 at 7 m. Sabsabi and Cielo [35] found that at various time delays for energies of 60 mJ, 100 mJ and 170 mJ, plasma temperatures of an Al alloy increased with increasing energy by ~500–1000 K. However, Yalcin et al. [34] studied aerosolized metals at five energies between 41 and 150 mJ at various time delays and found plasma temperatures to be not significantly different.

Temperatures for three powdered and pressed basalt geochemical reference materials (BEN, BHVO2, and GBW07105) were calculated using the Boltzmann plot method with 29 Ti II lines at 3, 5, and 7 m. Temperatures ranged from 13,900–14,400 K at 3 m, 13,800–14,400 K at 5 m, and 14,400–15,000 K at 7 m (Fig. 6); error bars are determined from the standard error of the Boltzmann plot slope. Results from the ChemCam data show no correlation with distance. For each sample, we find that the plasma temperatures at 3, 5, and 7 m are the same to within ~5%. Given the difficulty in calculating the temperature using ChemCam data, within the uncertainty of our measurements we cannot conclude that there is a relationship between plasma temperature and distance. Additional work is needed using a higher resolution gated spectrometer to reduce line overlap before any conclusions should be made.

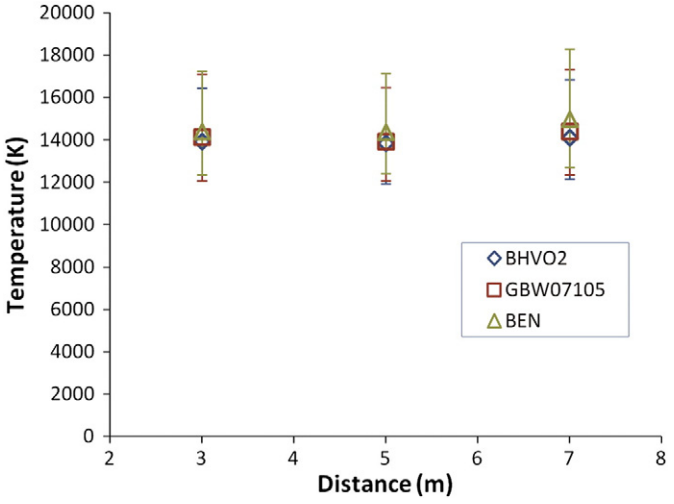

Fig. 6. Plasma temperature as a function of distance. Error bars are the calculated upper and lower bounds on the temperature based on the standard error of the Boltzmann plot slope. These results confirm that the relative ratios of peaks of the same element are statistically independent of distance.

3.3. Coupling efficiency

Different materials and different surface textures yield differing fluences of LIBS photons produced by the same laser beam. We refer to this as coupling efficiency. The standards used in this study coupled to the laser to varying degrees, with the strongest coupling material–the Ti plate used on the rover calibration target assembly for diagnostic purposes–providing about a factor of thirty more photons than the weakest coupling standard. Fig. 7a shows the relative coupling efficiencies in terms of total emission from peaks, obtained on Level 1 data (after dark subtraction, continuum removal, and instrument response correction) from the cleanroom 3 m data set (Test #6 in Table 1). Fig. 7b compares overall total emission including continuum, taken from the raw data. Titanium was not included in these plots, but was a factor of 3 higher than the strongest coupling geological standard. Anderson et al. [16] noted that the samples with the highest overall emission tended to be iron-rich samples. The overall concept is that optically dark minerals give excellent coupling, while low-iron, high-silica and high-alumina minerals such as quartz and kaolinite, which have high albedo, tend to couple poorly. However, the results in Fig. 7 indicate that some calcium and magnesium carbonates are also excellent LIBS emitters, and in fact, a dolomite (JDO1) is the strongest emitter with the continuum included and the aragonite (UNSAK) standard is third. The correlation between Fe abundance and overall emission is relatively weak. When considering only the total emission from atomic transitions, the iron and titanium-rich standard WM has the highest total radiance, at 3.2×10^{15} induced by each laser pulse, over the spectral range observed by ChemCam. A number of other iron-rich standards are nearly as strong in overall emission. However, some of the carbonate standards are still nearly as strong in overall coupling.

Another way to consider the coupling efficiency of a sample is to compare the signal strength of an emission line of an element that occurs in every sample observed in this environment: oxygen. There is a triplet that is not resolved by the ChemCam spectrometers at 777 nm. Fig. 7c shows the radiance in the highest channel for this peak (constitutes 24% of the radiance in the entire peak) for the standards in the cleanroom data set. The aragonite-rich standard (UNSAK) is 25% higher than the next highest standards, a basalt (SR688) and an olivine (DH4912) standard. Note that these differences represent chemical matrix effects, because aragonite does not have a higher oxygen fraction than other carbonates.

At the low end of each of the plots in Fig. 7 are three glasses (norite, shergottite, macusanite), while the picrite glass tends to couple better. The macusanite couples so poorly that it was omitted from several of the plots (see discussion below). The purest gypsum standard (GYPA) is also one of the poorest couplers. From a chemical composition point of view there is no rationale for why gypsum standards do not couple well: They are rich in calcium, similar to carbonates, and some sulfur-rich standards couple very well. However, poor coupling is consistently observed for relatively pure gypsum. For both the gypsum and the poor-coupling glass standards, in some cases the coupling degrades significantly over the course of successive laser shots. This was true both for the gypsum and for the natural glass standard, macusanite. For the latter standard, the first laser shot yielded a typical signal, but the second shot yielded only 15% of the intensity in the first, and by the ~20th shot there was less than 1% of the signal in each shot (Fig. 8). For this reason, the data for this standard were not processed. The overall emission level for the pure gypsum powder standard GYPA did not drop initially, but between shots 20 and 40 it dropped by about a factor of two. By comparison,

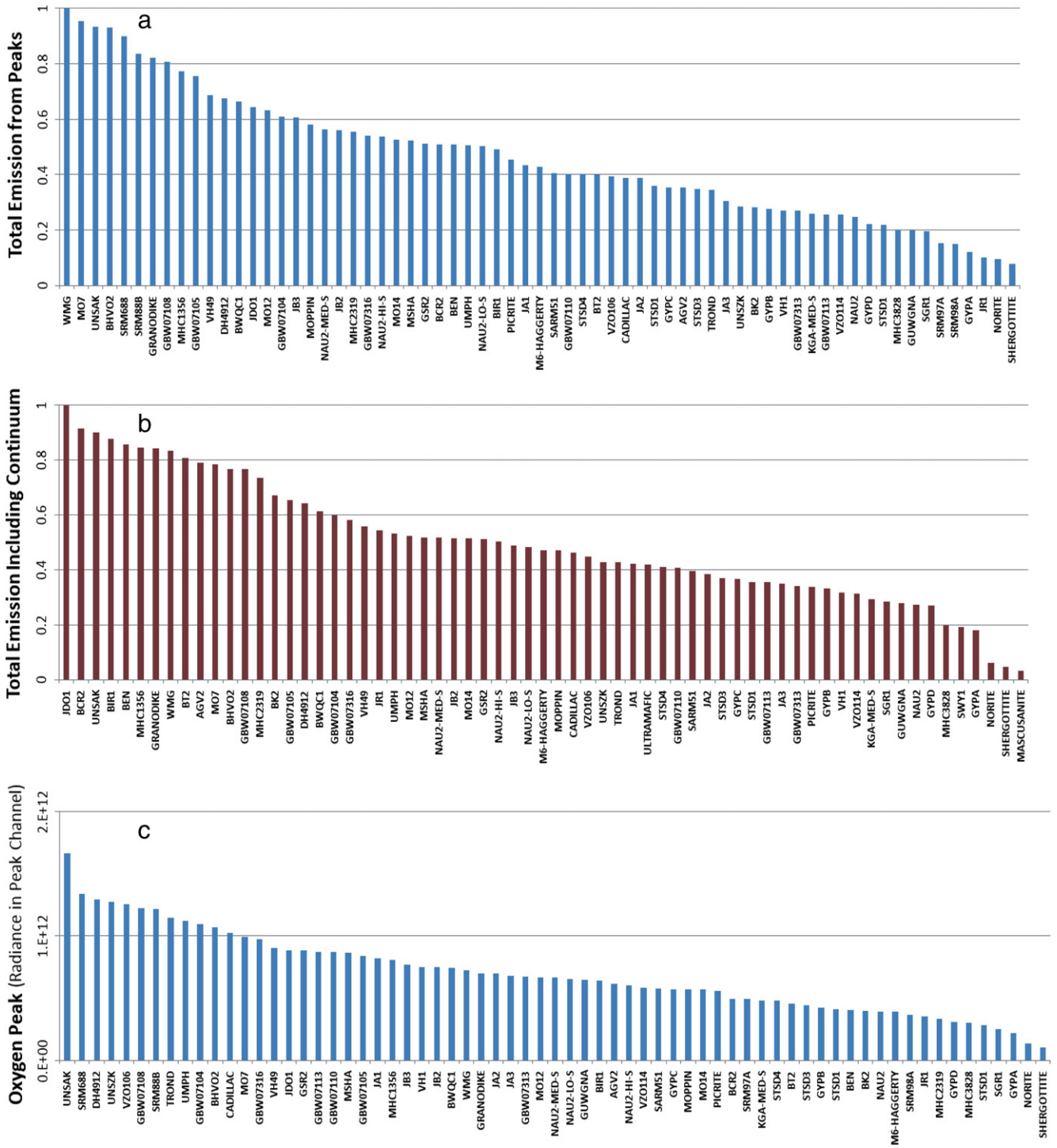

Fig. 7. Comparison of the emission from all peaks (a), total emission including continuum (b), and the peak channel of the oxygen 777 nm triplet (c) in the spectra collected by ChemCam during observations of the large group of standards at 3 m (#6 in Table 1). Macusanite was only included in the plot of total emission including continuum (b) due to the difficulty in coupling.

the shergottite synthetic glass did not lose any signal as the laser profiled into the material.

Among the four different locations probed for each standard, the standard deviation of the total emission was ~5% of the mean. There was no significant trend toward larger standard deviations with weaker overall emission with the possible exception of the standards with the very weakest emission (e.g., macusanite). Standard deviation is revisited later in the context of compositions obtained by LIBS, and the causes of the variations are determined in a few cases.

3.4. Emission line irradiances and detection limits

The unresolved oxygen triplet used in Fig. 7c constitutes the strongest peak in the spectrum of most samples observed in a simulated Mars atmosphere. Based on the discussion above, this triplet together can yield a radiance up to ~6.0×10^{12} photons/pulse/mm^2/sr/nm. On the low end of the range, ChemCam is sensitive to as few as 2000 photons entering its aperture, or a little over 10^7 total photons per pulse emitted at a distance of 3 m (the solid angle fraction of the ChemCam

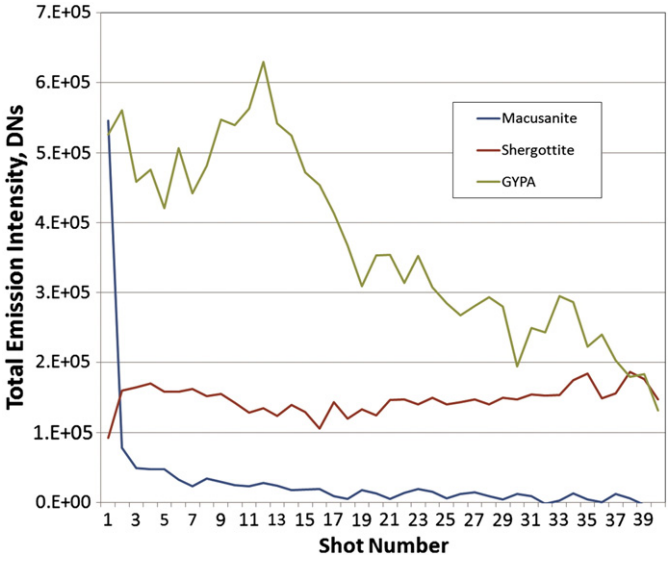

Fig. 8. Comparison of trends in total emission intensity in DNs (counts) over successive laser pulses on the same location of three targets displaying relatively weak coupling (e.g., Fig. 7).

110 mm diameter aperture is 1.7e−4) for optimum wavelengths near the center of the respective spectral ranges.

There are several ways in which ChemCam can be useful in terms of the elemental make-up of samples. One is to determine quantitative elemental abundances of major elements and of those minor and trace elements for which the signal is sufficient to do so. A second way is to determine the presence of elements for which the signal is low, but which can still be detected. To that end it is useful to understand the limits of detection (LOD) of a number of these elements. For this study we will follow the methods of Lasue et al. [38], who proposed three different criteria for detection limits:

1. The minimum abundance of a given element for which an emission peak can be clearly and systematically (for all replicates) identified above the white noise. This will be referred to as LOD 1. Note that for an ensemble of relatively few standards, this LOD may be relatively inaccurate and may be a conservative upper limit.
   This definition also lacks a rigorous criterion to tell what "significantly above the white noise" means. In this case we have taken a 3-sigma threshold above the white noise of a spectral region close to the peak of interest. A proper definition of a LOD should state what level of false negatives and false positives are accepted, and should be based on some estimate of the dispersion of blank measurements and on the dispersion obtained from measurements with concentrations being close to the LOD [39]. If only a probability of false positives is stated, it actually corresponds to a detection threshold.
2. In the case where a sufficient number of samples show a peak, i.e., are above the detection threshold estimated from LOD1, it is possible to determine a linear regression for the relationship between signal and elemental abundance. LOD 2 is determined from the slope and the standard deviation of the minimum detected composition. This can be written as $(\mathrm{LOD}\,2) = ksm$ where k is a factor that determines the probability of reporting false positives, s is the standard deviation of the measurements made at the lowest detected concentration, and m is the slope of the regression line. Again, this is really a detection threshold rather than a detection limit per se, because false negatives are not considered. A value of $k = 2$ is used in Table 2, corresponding to a two-sigma case, i.e., a confidence interval of 95% [5]. While this follows examples in recent literature [38,5], the method laid out by Currie [39] would use $k = 1.64$ to determine a detection threshold with a risk of 5% chance of false positives. This assumes no intercept in the regression line and no associated uncertainty, and no uncertainty associated with the slope of the regression line. It also assumes that the standard deviation of blank measurements can be obtained from repeated measurements of a target with low concentration. For LIBS measurements, where the continuum itself depends on the composition of the target and on some matrix effects, it is indeed difficult to achieve the conditions of a proper blank, as it should ideally give rise to the same continuum, but without the peaks of interest.
3. A final method taking into account all sources of variation involves calculating the slope and intercept values of the linear regression used in LOD 2, and using the uncertainties of these, projecting onto the y-axis the 95% confidence level curves defining the linear regression [40]. LOD 3 gives more rigorous detection limits than LODs 1 and 2, as it includes constraints on the probability of false negatives. This is particularly true for LIBS results in which the uncertainty of the linear regression is relatively high, as is the case in the data examined here.

Table 5
Limits of detection for selected minor and trace element emission lines.

Element	λ (nm)	LOD1		LOD2	LOD3	Correlation coefficient
		Standard	ppm	(ppm)	(ppm)	
H	656	Ultramafic	503	320	4966	0.75
Li	671	BHVO2	5	0.3	25	0.98
Cl	838	GBW07316	35,000			
K	766	JDO1	16	13	12,401	0.95
K	770	JDO1	16	12	12,195	0.95
Cr	425	BEN	360	9.7	445	0.58
Mn	403	NAU2MED-S	303	63	1330	0.90
Mn	294	SGR1	267	65	1465	0.88
Cu	327	GBW07313	424			
As	447	MCH2319	960			
Rb	780	STSD1	30	11	42	0.94
Sr	408	NAU2MED-S	95	15	358	0.95
Ba	455	JB2	208	46	973	0.82
Pb	406	MCH2319	300			

The data set used in this study is Test #1 in Table 1, with a distance of 3.0 m. This test gives slightly better results in terms of signal to noise than Test #6 in Table 1 due to the higher laser energy of ~14 mJ resulting from the cooler laser temperature, for which this unit was optimized. By contrast, the laser energy in test series #6 was ~10 mJ. A disadvantage was that Test series #1 involved fewer standards, which may have resulted in decreased regression line quality than an analysis using a larger number of standards. Table 5 gives the results for several relevant elements. For some of the peaks listed in this table only the lower abundances were used in the regressions: Li<151, Cr<500, Rb<170, and Sr<1800 ppm. Additionally, the K peak regressions were fitted with a polynomial to give slightly better fits. This is appropriate from a physical perspective, for example, if self-adsorption limits the emitted intensity from standards with the highest K contents. One outlier was removed from the Ba regression, which is most likely due to an interfering Ti emission line. One can see that LOD 3 is substantially higher than LOD 2 by factors between four and one thousand.

To complement the study done on the limited data set taken during thermal vacuum tests (Test #1 in Table 1), some minor peaks were identified in the spectra taken at room temperature on the larger group of standards, as some of these had higher minor and trace element abundances. For example, Cl was observed in samples with 3.5–4% abundances, Cu was observed in standards with 420 ppm or more of that element, Pb and As were observed at 300 and 960 ppm, respectively in the melanterite-bearing standard, and S was seen in a number of standards. These were added to Table 4, but only as LOD 1.

A few of the minor element peaks are shown in their contexts in Fig. 9. These peaks were taken from the spectral library corresponding

to Test #6 in Table 1. This figure displays the standards with the highest abundances of the elements in question. Boron is an important constituent of evaporite deposits, particularly in areas such as the southwestern U.S. where pegmatite weathering has contributed to the chemistry of the evaporites. The first panel of Fig. 9 shows the strongest B peak, at 249.85 nm, in this case at an abundance level of 23,107 ppm in KGA-MED-S, which, like the other ceramics, was made with lithium tetraborate to promote sintering.

Sulfur analysis with LIBS has been the focus of a number of papers that studied this element either under a simulated Mars atmosphere [41,14] or in other ambient gases (e.g., [42,43]). Detection of S seems quite strongly affected by the laser energy, which is lower for ChemCam than for many other applications. At energies of ~10 mJ we observe that the strongest S peaks in the ChemCam spectral range (240–850 nm) are in the 542–550 nm range, shown in Fig. 9b for gypsum standards GYPB and GYPA (SO_3 = 41 and 46.2%, respectively). The presence of multiple unresolved emission lines results in broad peaks at 543.02/543.43 and 547.51/547.65/547.97 nm, while a single peak exists at 545.53 nm.

The strongest Cl peak is shown at 837.82 nm for GBW07316 (35,000 ppm) and GBW07313 (40,700 ppm), in contrast to SRM88B, which as a limestone, has essentially no Cl (Fig. 9c). Fig. 9d shows Cr peaks at 425.56 and 427.60 nm observed in the synthetic picrite glass standard (2588 ppm Cr). Copper is shown in Fig. 9e; at an abundance of 643 ppm in VZO106 only the peak at 327.49 nm is seen. Another strong Cu line is usually observed at 324.85 nm, but it is partially masked by an interfering Ti emission line. On Earth a common occurrence of Cu is in sulfate minerals. Due to the higher abundance of S on the Mars surface, it is possible that elements typically combining with sulfur might be found. Another such element is As. Peaks of As II are shown in Fig. 9f at 445.97, 446.23, 446.76, 447.57 and 449.55 nm, observed in the melanterite-bearing standard MHC2319, where its abundance is 965 ppm.

Rubidium peaks are observed in a number of standards high in silica and alkalis. The example shown in Fig. 9g, GUWGNA, has 2020 ppm of Rb. The Rb peak at 794.98 nm has an oxygen interference centered directly under it; the Rb peak at 780.24 nm supposedly has an Si I interference centered at 780.22 nm, but one can see from the AGV2 trace that it is quite a minor interference. For reference, AGV2 has only 66 ppm Rb.

LIBS is relatively sensitive to Ba, the strongest peak for which is shown at 455.53 nm in Fig. 9h as observed in GBW07313, which contains 4400 ppm of Ba. For comparison, basalt BIR1 has only 7 ppm of Ba, but shows that Ti emission peaks at 455.10, 455.37, and 455.68 nm can interfere with the Ba peak. The final panel of Fig. 9 shows a Pb I peak at 405.90 nm as observed in SARM51, which contains 5200 ppm of Pb. The Pb peak is surrounded by Fe peaks; however, these should be resolvable from Pb.

Carbon presents a different challenge because of its presence in the Mars atmosphere. The LIBS sparks ionize some of the atmospheric species, and hence carbon is observed in all of the standards analyzed in the simulated Mars atmosphere of 930 Pa of CO_2, as pointed out in an extensive study of carbon peaks from these spectral libraries [44]. Simply performing a linear regression, as done for the rest of the peaks in Table 5, gives a LOD 2 of nearly 20 wt.%. However, by plotting the carbon peak intensity against that of the oxygen peak, one can see that standards with sufficient carbon depart from the trend produced by samples with no inherent carbon. By taking the deviations of carbon-bearing standards from the non-carbon trend, an LOD 2 of 2.4 wt.% and an LOD 3 of 6.0 wt.% can be obtained.

3.5. Quantitative abundance determinations using multivariate analysis

The Level 1 processed data described in Section 2 were used to build a multivariate analysis training set using the standards in Test #6 in Table 1. An IDL-based partial least squares (PLS) algorithm [45] was applied to yield compositional abundances (e.g., Fig. 1). The specific algorithm used here is known as PLS2, which fits all elements simultaneously rather than each element separately (PLS1). For use with Mars data the edges of the spectral ranges were masked so that regions with the lowest signal-to-noise were not used. Masked regions included $\lambda < 246.8$ nm and $\lambda > 338.5$ nm in the UV (163 pixels masked), $\lambda < 387.9$ nm in the VIO region (120 pixels masked), and $\lambda < 492.5$ nm and $\lambda > 849.2$ nm in the VNIR region (373 pixels masked). However, for the results presented here the masking was not used. It did not make much difference for the current analysis using data taken at 3 m; however, it improved the results once the Martian instrument response was applied and for longer distance measurements. The results were obtained using eleven principal components, which was selected because this number gave the best overall results averaged across all major elements. This is clearly a compromise, as some elements are fit better with fewer principal components while other elements with more emission lines are fit better with more components. A strong argument for using PLS1 in future analysis is the ability to optimize each element separately, which in some cases significantly improves the accuracy at the expense of longer overall run times.

The quality of the abundance determinations was assessed using a leave-one-out cross-validation, in which the model is successively built with one standard missing each time, then used to estimate the composition of the missing standard, and finally comparing it against the known composition. This was done for all of the standards. Note that four spectra exist for each standard, and so all four were left out. The predicted compositions for all four spectral observations of that standard were then averaged. The differences from the known compositions are given in Table 6, and the standard deviations of the four predicted abundances for each standard are given in Table 7.

The uncertainty of any sample lying in the compositional range covered by the standards is estimated from the root mean square error product (RMSEP), which describes the accuracy of the measurements, and the standard deviation, which measures precision. These two quantities can be quite different for LIBS analyses, as shown by the overall differences between Table 6 (representing accuracy) and Table 7 (precision). The mean precision for SiO_2 in these standards, given by the mean of the first data column in Table 7, is ±1.2 wt.%, however, the accuracy is not as good, as shown by Table 6. The RMSEP has been described and used in a number of recent works on LIBS quantification [11,13,15–17,38,46]. It is calculated by the following expression:

$$\mathrm{RMSEP} = \sqrt{\frac{1}{n}\sum_{i=1}^{n}\left(y_{ip} - y_i\right)^2} \tag{6}$$

where n is the number of samples, y_{ip} is the estimated abundance of sample i and y_i is its actual composition. The RMSEP is given in the same units as the estimated quantity, in this case weight percent (wt.%). The RMSEP values for the major elements in the training set derived from the large-group analysis (Table 1, Test 6) are given at the bottom of Table 6. Overall, many of the errors of the individual standards are large, leading to a higher than desired RMSEP. In the next section we will investigate sources of error and will then discuss methods for significantly reducing the errors.

3.5.1. Repeatability of composition estimates

By examining the results of the standard deviations (Table 7) and the leave-one-out calculations themselves (Table 6) in detail, we can understand some of the reasons for the errors. We look first at the repeatability of the estimated abundances of each standard over the four observation points per standard. We will refer to this as precision. Then we will investigate high-precision, low-accuracy results.

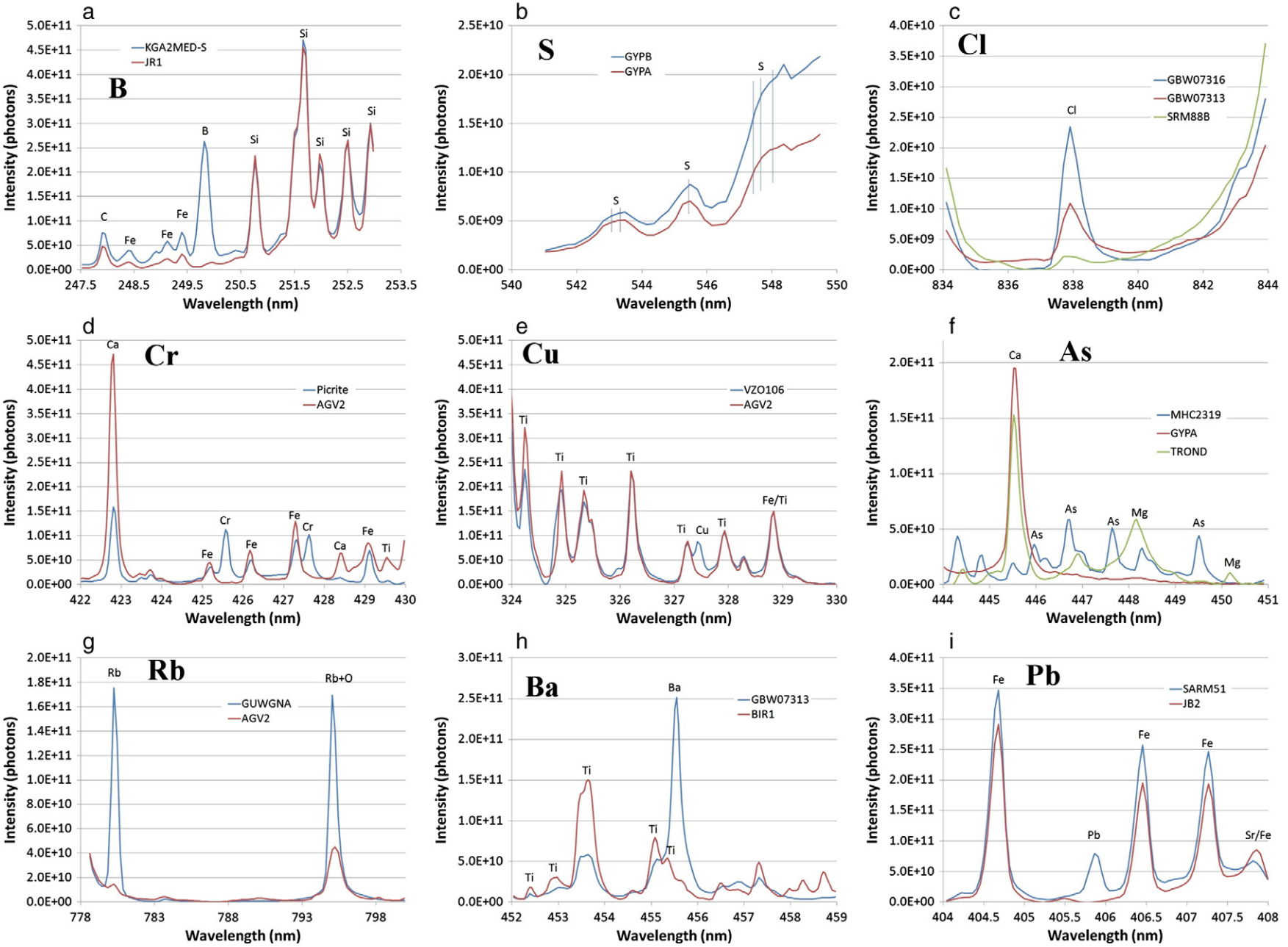

Fig. 9. Spectral regions showing selected minor and trace element peaks respectively for B (KGA-MED-S = 23,107 ppm), S (GYPA = 46.2, GYPB = 41 wt.% SO_3), Cl (GBW07316 = 35,000, GBW07313 = 40,700 ppm), Cr (picrite = 2590 ppm), Cu (VZO106 = 640 ppm), As (MHC2319 = 970 ppm), Rb (GUWGNA = 2020 ppm), Ba (GBW07313 = 4400 ppm), and Pb (SARM51 = 5200 ppm). In each case one or two standards rich in the given element is/are plotted, in most cases along with one or more standards poor in the same element so the trace peak can be distinguished from the surrounding peaks.

The bottom two rows of Table 7 give the mean and median standard deviations, respectively. The mean standard deviations are factors of five to twenty below the RMSEPs given for each element at the bottom of Table 6. This confirms that the measurements yield relatively repeatable results and that precision does not contribute significantly to the overall errors. We will still briefly investigate the standards with the poorest precision.

The standard with the largest standard deviation is MHC3828 (Table 7), whose third point differs significantly from the other two. Further inspection of these indicates that the intensities of the spectra from all observations but the one in question drop significantly over the course of the 40 laser shots. This standard is an impure gypsum, and it appears that there is heterogeneity in the pressed powder. As described above, pure gypsum does not couple well with the laser. The interrogation in question appears to have hit an area with a higher abundance of impurities; its composition differed slightly and the LIBS intensity did not drop significantly over the course of the 40 spectra. The same phenomenon was observed in GYPD, another impure gypsum standard, in which the overall intensity of the fourth point did not drop in intensity nearly as much as the rest of the points; in addition to having an overall stronger intensity, it clearly maintained stronger iron peaks throughout the course of the 40 laser shots. Three other gypsum standards, GYPA, GYPB, and GYPC, are more pure and did not display unusually high spectral standard deviations (Table 7). It is possible that the impure gypsum standards exhibit a fractionation between material which couples well with the laser and the pure gypsum which does not couple well.

In addition to the gypsum standards, the rhyolite standard VH1 was found to have an unusually high standard deviation between the four observations. Comparing all 40 spectra of the third observation point shows a bimodal distribution in which Si decreased and Fe increased during the course of the observation. Several other standards appear to display more subtle variations: BK2 appears to have a slight compositional difference in its first analysis point relative to the others; in VZO114 the signal appears to decrease at a slightly different rate for Si than for the other elements.

We make two preliminary conclusions here: One is that the precision of LIBS on a single homogeneous material–that is, the precision of the technique itself–is many times better than the RMSEP, which is a measure of the accuracy. The instrumental precision is at least on the order of the mean standard deviations in Table 7, and likely somewhat better when the above standard heterogeneities are taken into account. This means that within a given rock ChemCam will be able to search for minute chemical variations far below the level of the RMSEP, for example, in observing different layers in a stratified sandstone or mudstone outcrop. A second preliminary conclusion is that heterogeneity of the standard powders is, in just a few cases, a significant source of spectral heterogeneity and hence, contributes to a higher RMSEP. The observation of spectral heterogeneity stemming from compositional variations in rock powder standards, many with quantified grain sizes less than 20–60 μm, seems somewhat surprising at first. After all, the laser beam typically bores roughly on the order of 1 mm into the pellets during the 40 shots, which is tens to hundreds of grain diameters deep, i.e., each laser shot tends to remove several grains in depth, and the beam diameter of ~350 μm, which is tens to hundreds of grains in cross section. However, a recent study [47] indicated that in rock samples, LIBS tends to be sensitive to mineral grains at a scale somewhat smaller than the beam diameter.

3.5.2. Contributors to PLS inaccuracy

Now we will look at the errors not attributable to precision issues. In general, samples that have significantly above-average abundance of a given element will be under-predicted and samples that are deficient in an element will be over-predicted. This is shown most clearly for low-abundance elements such as TiO_2 and MnO, for which the PLS model relies heavily on emission lines other than those from the element of interest (Fig. 10). However, the PLS model for all elements relies to some extent on emission lines from elements other than the one being predicted, and the trend of increasing error with compositions farther from the mean is apparent to some degree for most of the major elements. This is affected by the distribution of elemental abundances, which is not constant in the training set. The model will be biased toward optimal predictions for samples with compositions in a range that is well represented in the training set. Samples that are outliers have less weight in the overall model, and are thus less well predicted.

There are a number of examples in which the reason for inaccuracy can be deduced from studying the loadings to see how much emission lines attributable to other elements play a role in the abundance determinations of a given element. These cases are typically drawn from compositional outliers, where loadings of other element emission lines that might make sense for the bulk of the training set do not apply correctly to the more extreme compositions.

The olivine sample DH4912 prediction overestimates the amount of Fe_2O_3, CaO, and TiO_2 in the sample, while underestimating Al_2O_3 and MnO. DH4912 has the highest MgO content in the data set, and the PLS models for Fe_2O_3, TiO_2, and CaO all have positive regression coefficients that correspond to Mg emission lines. The predicted Al_2O_3 content is actually negative for this target, likely because of the negative regression coefficients corresponding to the Si emission line at 288 nm and the K lines at 766 and 770 nm. These lines are relatively weak in the DH4912 spectrum, but the spectrum also lacks most of the lines with positive regression coefficients in the Al_2O_3 model, leading to a net negative prediction.

The sample BEN is a low-SiO_2 basalt containing feldspathoid minerals. The PLS model overestimates the SiO_2 content of BEN by ~9.5 wt. %. This overestimate is not unexpected: the model is trained primarily on igneous rocks containing feldspar minerals. Feldspathoid minerals are chemically similar to feldspars but have lower SiO_2 contents. Because the PLS model responds to emission lines other than SiO_2, it overestimates the SiO_2 content of BEN.

Granodike is a low-SiO_2 trachybasalt with a Na_2O content of 4.51 wt.%. For comparison, the highest Na_2O content in the cleanroom data set is 5.91%. The PLS model underestimates the Na_2O content of Granodike, likely because the sample's spectrum shows relatively weak Na emission compared to the Na_2O content, as shown in Fig. 11. A similar example, but in the opposite sense, is found in the K_2O abundance of GUWGNA. In this case the K is significantly overestimated based on anomalously high peak heights for this K abundance. These are examples of chemical matrix effects, where some feature of the sample chemistry apparently prevents the expected Na transition intensity, or boosts the K transition intensity, relative to that expected for the respective abundances. In these cases, compositional estimates using peak area ratios would also not give the correct result. However, a PLS training set that included other similar standards displaying this same effect would presumably yield an accurate result. Further analysis of the PLS results are given in the supporting online material.

3.5.3. Steps to improve PLS accuracy

There are a number of steps that can be carried out to improve the accuracy of composition estimates derived from the training set obtained in this study. These include culling standards that are far from the compositional range of the Mars samples and from the bulk of the standards. Most of the standards were selected in anticipation of the Mars compositional range, but prior to landing this range was not known. On the other hand, it is relatively easy to determine which standards are outliers relative to the main body of standards. This will be discussed in the next section. Additional gains are certain to be made by increasing the number of standards used in the database. This will involve using instruments designed to mimic the

Table 6
ChemCam LIBS errors in wt.% for oxides of major elements, from data set #6 in Table 1. Negative values indicate overestimation; positive values are underestimates relative to the actual values given in Table 3.

	Mean errors									Error sum	Mean sum LIBS	Sum actual
	SiO_2	TiO_2	Al_2O_3	Fe_2O_3T	MnO	MgO	CaO	Na_2O	K_2O			
AGV2	0.84	−0.38	3.30	−2.44	−0.09	−0.18	−0.03	0.00	0.47	7.74	96.62	98.11
BCR2	3.79	−0.09	0.52	0.51	0.01	−1.62	−0.85	−0.20	0.16	7.77	97.28	99.52
BEN	−9.46	0.48	−0.46	−0.88	0.02	5.01	3.53	−0.10	−0.07	20.01	97.50	95.57
BHVO2	2.92	1.01	−0.93	2.53	0.00	1.54	1.86	−0.14	0.05	10.99	91.12	99.97
BIR1	4.82	−0.11	2.20	−2.11	0.07	0.07	2.95	−0.76	0.03	13.12	93.37	100.51
BK2	2.81	0.01	5.34	4.09	−0.02	−5.31	−2.44	−0.10	−0.14	20.26	95.08	99.31
BT2	−0.83	−0.44	2.80	−1.26	−0.02	−2.08	−0.13	0.93	−0.08	8.58	99.01	97.89
BWQC1	4.11	0.42	−0.90	2.80	0.12	−1.61	−1.76	1.89	0.35	13.96	93.93	99.36
CADILLAC	1.71	0.01	−0.87	−4.11	−0.03	2.32	−0.36	0.74	0.94	11.08	98.93	99.29
DH4912	7.76	−3.20	7.18	−16.63	0.38	−0.92	−12.22	1.31	0.53	50.12	114.44	98.63
GBW07104	12.41	0.03	3.42	−2.96	−0.07	−1.27	−3.34	0.92	0.61	25.04	85.20	94.95
GBW07105	−6.04	0.45	0.94	3.56	−0.02	1.21	1.05	0.65	0.91	14.82	93.98	96.69
GBW07108	−0.98	0.06	0.20	0.38	−0.02	2.03	5.71	−0.16	0.38	9.93	57.65	65.25
GBW07110	−3.80	−0.13	2.22	−0.50	−0.09	1.70	0.64	−0.28	1.73	11.08	94.82	96.31
GBW07113	−7.24	−0.04	−4.29	1.34	0.04	3.41	2.78	−1.37	0.93	21.43	102.58	98.14
GBW07313	−4.71	0.50	−2.54	2.58	0.36	−0.84	2.32	−0.07	−0.79	14.71	91.31	88.14
GBW07316	−4.27	0.24	1.24	1.98	0.29	0.83	2.98	0.66	−0.13	12.61	70.35	74.17
Granodike	1.61	1.18	−0.27	1.09	0.09	−1.86	−0.80	2.14	0.09	9.13	95.70	98.98
GSR2	9.54	−0.13	3.29	−3.72	−0.08	−1.79	−3.64	0.80	0.45	23.45	90.25	94.96
GUWGNA	17.17	−0.12	−0.36	−1.72	0.20	4.40	−2.28	0.22	−1.46	27.93	79.60	95.64
GYPA	2.52	0.18	1.93	1.47	0.06	−0.13	−11.33	0.38	0.06	18.07	38.57	33.71
GYPB	6.57	0.18	−2.89	0.14	−0.06	−4.66	−0.27	0.03	0.02	14.84	36.92	35.97
GYPC	0.37	0.13	−3.97	0.65	−0.09	−1.92	0.94	−0.05	0.24	8.38	44.56	40.87
GYPD	−16.59	−0.28	−2.80	−2.74	−0.08	−1.34	5.68	−0.46	−0.59	30.55	61.65	42.46
JA1	3.55	0.02	−0.86	−1.67	0.02	0.48	−0.58	0.16	−0.53	7.87	98.48	99.08
JA2	5.11	−0.38	2.51	1.29	−0.07	−3.37	−0.84	−0.08	−0.26	13.90	93.75	97.66
JA3	2.92	0.32	2.10	1.19	−0.04	0.20	0.28	−0.48	−0.84	8.35	94.08	99.72
JB2	−0.43	0.03	0.93	2.14	0.07	1.64	0.52	−0.35	−0.08	6.18	96.11	100.57
JB3	0.48	−0.09	2.93	0.15	0.02	−0.29	0.30	0.47	0.18	4.91	95.94	100.08
JDO1	2.55	−0.10	−4.37	−3.40	−0.08	7.06	2.94	0.13	0.74	21.37	47.38	52.85
JR1	0.34	0.24	−5.35	−1.00	0.07	1.16	1.94	0.28	1.04	11.43	99.90	98.62
KGA-MED-S	6.52	0.13	6.71	−1.84	−0.06	−3.62	−4.51	0.04	0.71	24.13	74.10	78.17
M6-HAGGERTY	0.59	3.40	−10.20	5.92	−0.01	12.73	−5.94	−1.61	−0.41	40.82	92.23	96.70
MHC1356	−3.03	0.30	2.99	15.48	−0.08	−1.03	−0.79	0.56	−0.05	24.31	80.16	94.50
MHC2319	29.13	−0.41	2.08	−24.74	−0.02	−1.36	−6.07	0.32	−0.32	64.45	88.96	87.58
MHC3828	−9.46	−0.46	−3.62	−0.65	−0.14	−5.20	3.98	−0.53	−0.65	24.68	60.11	43.39
MO12	−0.95	−0.54	3.19	−2.56	−0.02	−2.26	−0.24	0.93	0.10	10.78	102.32	99.98
MO14	−0.69	−0.22	3.53	−2.20	0.01	−3.64	−0.96	0.63	−0.03	11.91	101.21	97.64
MO7	−7.67	1.39	5.62	2.79	−0.02	0.13	4.73	−0.15	−0.38	22.88	91.73	98.16
MOPPIN	1.50	−0.21	−15.04	−1.15	0.23	−1.27	−2.22	0.14	−0.06	21.83	101.43	98.97
MSHA	6.02	−0.72	1.55	−7.72	−0.06	−2.07	−1.00	1.37	0.17	20.68	102.33	99.87
NAU2	−12.51	0.63	−2.77	14.34	−0.09	0.78	0.04	−1.33	−1.00	33.49	91.08	89.16
NAU2-HI-S	−9.75	−0.09	−1.82	−5.28	−0.09	−0.92	7.70	0.38	0.70	26.73	79.94	70.77
NAU2-LO-S	6.14	0.22	0.86	1.55	−0.05	−0.20	−2.13	0.48	0.39	12.01	78.39	85.65
NAU2-MED-S	−1.30	−0.02	−0.53	−1.42	−0.07	−0.33	2.06	0.40	0.57	6.70	79.12	78.49
Norite	2.22	0.56	−0.81	3.30	−0.04	1.80	−4.41	−1.75	−0.04	14.92	103.81	104.65
Picrite	−10.06	−0.07	1.32	7.18	−0.10	0.01	−0.08	−0.05	−0.27	19.14	104.60	102.47
SARM51	−21.11	0.29	−0.92	2.34	0.12	1.76	−1.08	−0.52	−0.46	28.61	86.84	67.25
SGR1	−7.79	−0.50	−0.47	−2.77	−0.21	2.67	−1.75	0.15	−0.35	16.66	66.58	55.56
Shergottite	0.87	0.24	−1.51	6.78	−0.06	1.65	−2.59	−1.86	−0.54	16.11	98.46	101.44
SRM688	1.72	−0.21	3.44	−0.89	0.03	−2.21	0.98	−0.09	0.01	9.61	97.57	100.36
SRM88B	−7.63	−0.31	−4.64	−4.02	−0.08	8.02	3.64	−0.19	0.20	28.72	57.90	52.89
SRM97A	−4.81	0.03	0.80	−2.57	−0.04	−1.30	2.42	−0.08	−0.07	12.11	91.23	85.61
SRM98A	0.70	−0.27	1.35	0.69	−0.10	−0.05	−0.40	−1.00	−1.12	5.68	87.13	86.93
STSD1	−0.47	0.09	0.40	−5.08	0.36	0.07	−3.11	0.06	0.01	9.65	75.72	68.06
STSD3	3.40	−0.08	1.13	−2.72	0.14	0.07	−1.79	−0.22	−0.06	9.62	75.63	75.50
STSD1	11.36	0.00	2.09	3.76	0.32	−0.88	−7.11	−1.37	−0.80	27.70	60.68	68.06
STSD4	11.07	−0.26	1.05	−3.47	0.03	−0.66	−2.99	0.22	−0.17	19.92	83.29	88.10
Trond	3.66	0.02	0.22	1.11	−0.11	−0.23	−0.96	1.42	−2.29	10.01	97.33	100.16
UMPH	−7.42	−0.14	5.73	−3.67	−0.10	−0.10	−0.33	1.53	2.93	21.97	101.36	99.78
UNSAK	1.48	0.15	12.83	2.60	0.20	−0.57	9.12	1.12	−0.72	28.79	29.77	55.97
UNSZK	−9.32	0.25	−2.59	−1.53	−0.02	3.13	2.74	0.75	−0.20	20.53	106.23	99.44
VH1	8.42	−0.63	0.84	0.85	−0.14	−4.57	0.76	0.37	0.81	17.39	93.46	100.17
VH49	−1.52	−0.43	6.05	−2.64	0.02	−2.66	0.42	0.14	−0.35	14.24	100.84	99.86
VZO106	−5.03	−0.43	−11.59	−9.92	−0.20	0.22	4.85	−2.99	−2.17	37.40	108.69	81.43
VZO114	4.39	−0.95	−9.27	1.84	−0.09	−0.02	−7.48	−1.80	−0.72	26.55	79.08	64.97
WM	−5.23	−2.75	−6.87	4.35	−0.03	3.78	7.01	−2.25	−0.58	32.85	96.68	97.86
RMSEP	**7.73**	**0.79**	**4.44**	**5.76**	**0.13**	**3.03**	**3.97**	**0.97**	**0.79**			

output of ChemCam, as will be discussed later. Improvements might be realized by removing the standards mentioned above which have large standard deviations.

3.5.3.1. Removing outliers using independent component analysis. We determine outliers in the PLS training model by calculating the distance between the spectra in the training set and an unknown sample

Table 7
Standard deviations of abundance estimates from the four analysis points for each standard, in wt.%.

	Standard deviations ($N=4$)									Std. dev. of sum pred.
	SiO_2	TiO_2	Al_2O_3	Fe_2O_3T	MnO	MgO	CaO	Na_2O	K_2O	
AGV2	0.500	0.108	0.252	0.496	0.006	0.282	0.247	0.102	0.135	1.156
BCR2	0.547	0.084	0.127	0.325	0.002	0.289	0.098	0.060	0.056	0.314
BEN	0.257	0.059	0.167	0.397	0.003	0.478	0.196	0.074	0.041	0.487
BHVO2	0.165	0.129	0.166	0.510	0.002	0.355	0.186	0.038	0.032	0.330
BIR1	1.035	0.151	0.360	0.393	0.007	0.791	0.601	0.019	0.029	1.490
BK2	0.597	0.545	1.785	0.685	0.025	1.858	0.317	0.253	0.808	0.893
BT2	0.834	0.282	1.177	0.550	0.009	1.423	0.479	0.151	0.153	0.748
BWQC1	1.251	0.265	0.716	0.394	0.006	0.842	0.806	0.261	0.172	1.429
CADILLAC	1.392	0.129	0.687	1.216	0.013	0.319	0.507	0.148	0.166	0.791
DH4912	1.126	0.070	0.187	0.492	0.004	0.577	0.177	0.036	0.028	2.437
GBW07104	0.459	0.051	0.289	0.131	0.002	0.143	0.185	0.011	0.016	0.672
GBW07105	0.487	0.034	0.166	0.170	0.004	0.458	0.126	0.052	0.040	0.648
GBW07108	1.476	0.035	0.259	0.905	0.005	0.295	1.034	0.017	0.108	1.114
GBW07110	1.393	0.107	0.303	2.047	0.006	0.177	0.317	0.196	0.319	0.176
GBW07113	1.889	0.147	0.320	0.779	0.009	0.228	0.150	0.067	0.168	1.044
GBW07313	1.346	0.031	0.098	0.078	0.002	0.172	0.288	0.395	0.045	1.437
GBW07316	0.483	0.024	0.152	0.049	0.003	0.125	0.390	0.166	0.040	0.332
Granodike	2.560	0.425	0.364	1.348	0.008	1.047	0.405	0.324	0.116	1.756
GSR2	0.622	0.069	0.234	0.401	0.007	0.208	0.294	0.075	0.070	0.891
GUWGNA	0.559	0.030	0.394	0.330	0.010	0.205	0.101	0.039	0.073	0.611
GYPA	0.668	0.044	0.310	0.401	0.005	0.121	0.662	0.028	0.011	0.634
GYPB	0.839	0.022	0.286	0.245	0.002	0.470	0.703	0.071	0.025	1.005
GYPC	0.435	0.038	0.161	0.113	0.003	0.429	0.484	0.016	0.039	0.624
GYPD	6.892	0.079	0.759	4.451	0.014	1.583	3.465	0.066	0.206	6.375
JA1	0.537	0.094	0.204	0.473	0.004	0.190	0.359	0.078	0.059	0.375
JA2	0.370	0.052	0.119	0.128	0.002	0.208	0.177	0.064	0.075	0.467
JA3	0.843	0.135	0.246	0.914	0.005	0.324	0.191	0.134	0.120	0.743
JB2	0.472	0.083	0.162	0.500	0.004	0.293	0.329	0.048	0.013	0.610
JB3	0.985	0.158	0.395	0.367	0.011	0.332	0.937	0.056	0.058	1.008
JDO1	0.152	0.005	0.020	0.058	0.001	0.050	0.100	0.006	0.006	0.239
JR1	2.414	0.192	0.937	0.806	0.014	0.252	0.617	0.170	0.179	2.344
KGA-MED-S	0.741	0.023	0.341	0.271	0.003	0.228	0.304	0.035	0.038	0.608
M6-HAGGERTY	0.410	0.179	0.763	0.524	0.006	1.876	0.310	0.108	0.063	1.738
MHC1356	1.846	0.100	0.326	0.774	0.003	0.082	0.812	0.044	0.172	0.741
MHC2319	0.878	0.076	0.131	0.486	0.003	0.197	0.284	0.014	0.047	0.940
MHC3828	11.143	0.416	1.766	0.408	0.057	3.017	6.371	0.338	0.942	11.230
MO12	1.202	0.284	0.809	1.537	0.008	0.693	0.418	0.250	0.079	0.977
MO14	0.758	0.322	0.133	0.806	0.010	0.478	0.864	0.065	0.059	0.752
MO7	0.962	0.185	0.579	0.930	0.002	0.322	1.442	0.083	0.088	1.015
MOPPIN	0.551	0.106	0.219	0.459	0.001	0.098	0.538	0.089	0.028	0.635
MSHA	0.934	0.211	0.400	0.863	0.010	0.740	0.431	0.115	0.078	0.561
NAU2	0.606	0.072	0.170	0.221	0.002	0.178	0.252	0.029	0.028	0.999
NAU2-HI-S	0.703	0.061	0.130	0.480	0.001	0.064	0.404	0.022	0.011	0.182
NAU2-LO-S	0.514	0.023	0.107	0.449	0.002	0.131	0.242	0.031	0.031	0.294
NAU2-MED-S	0.563	0.035	0.158	0.293	0.002	0.131	0.245	0.026	0.038	0.686
Norite	0.901	0.040	0.430	0.169	0.004	0.090	0.307	0.054	0.080	1.187
Picrite	0.417	0.054	0.375	0.401	0.006	0.500	0.557	0.216	0.106	0.980
SARM51	0.412	0.115	0.171	0.161	0.004	0.396	0.173	0.047	0.060	0.757
SGR1	2.722	0.023	0.406	2.182	0.011	0.426	0.810	0.103	0.144	3.398
Shergottite	0.444	0.021	0.221	0.111	0.002	0.040	0.114	0.018	0.016	0.445
SRM688	1.093	0.329	0.670	0.495	0.014	2.246	1.049	0.182	0.105	0.865
SRM88B	0.219	0.012	0.043	0.173	0.003	0.101	0.312	0.022	0.033	0.691
SRM97A	0.471	0.081	0.112	0.255	0.003	0.210	0.200	0.022	0.054	0.591
SRM98A	0.623	0.073	0.562	0.478	0.006	0.250	0.061	0.039	0.065	1.006
STSD1	0.445	0.046	0.176	0.105	0.001	0.170	0.212	0.027	0.046	0.794
STSD3	0.737	0.077	0.388	0.137	0.004	0.066	0.150	0.094	0.098	1.152
STSD1	1.238	0.036	0.255	0.521	0.004	0.337	0.778	0.126	0.143	0.468
STSD4	0.600	0.096	0.187	0.445	0.005	0.085	0.581	0.055	0.028	0.661
Trond	0.544	0.082	0.286	0.231	0.010	0.452	0.284	0.062	0.212	0.399
UMPH	0.709	0.262	0.759	0.300	0.007	0.139	0.142	0.074	0.232	0.723
UNSAK	0.139	0.010	0.236	0.111	0.003	0.051	0.291	0.006	0.035	0.084
UNSZK	1.454	0.186	0.547	0.427	0.011	0.162	0.142	0.056	0.100	0.872
VH1	4.983	0.730	1.536	1.087	0.038	2.795	1.383	0.503	0.547	1.356
VH49	1.113	0.254	0.832	0.660	0.005	1.158	0.759	0.031	0.056	1.028
VZO106	0.354	0.081	0.261	0.582	0.006	0.476	0.173	0.227	0.024	0.576
VZO114	4.487	0.160	2.232	0.189	0.013	0.210	3.279	0.293	0.129	3.914
WM	0.863	0.118	0.241	0.282	0.003	0.237	0.128	0.058	0.053	0.545
Mean	**1.201**	**0.129**	**0.430**	**0.568**	**0.007**	**0.498**	**0.595**	**0.101**	**0.112**	**1.151**
Median	**0.709**	**0.082**	**0.286**	**0.427**	**0.005**	**0.282**	**0.312**	**0.064**	**0.060**	**0.752**

(one of the standards). We remove the standards that are the least similar to the unknown sample one by one to check the effect of outliers on the PLS predictions. Each time a standard is removed, a PLS model is re-calculated, optimized, and its prediction accuracy is checked; it is assumed that the training model is adequate to predict the unknown standard. We used independent component analysis

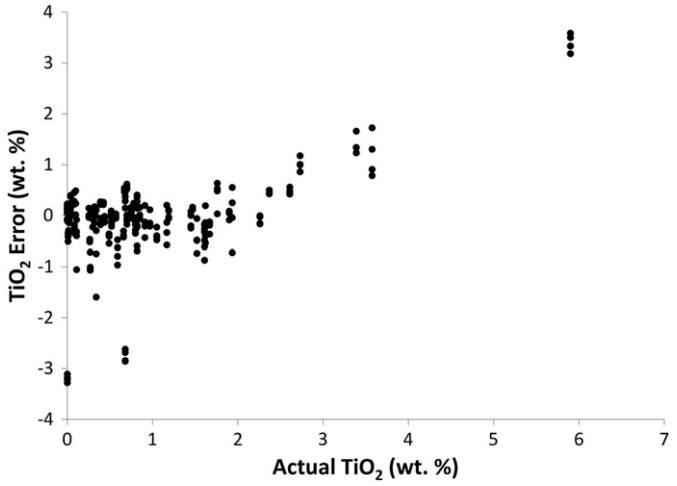

Fig. 10. Error in the predicted TiO_2 content plotted against the actual TiO_2 content of standards.

(ICA) [48–51] to determine the distance in spectral phase space in three different ways:

1. Euclidean distance calculated in the original 6144-dimensional spectral space.
2. Euclidean distance calculated in an ICA reduced 10-dimensional space.
3. Mahalanobis distance calculated in an ICA reduced 4-dimensional space. Four is the maximum number of dimensions in this case because we have only four spectra per standard.

Standards are successively removed, largest distance first, up to the 56th one, leaving only ten. No more were removed because PLS models clearly yield worse results when only ten standards remain in a training set used to predict all of the major elements. The results of Case 1 (Euclidean distance in 6144-dimensional space) are described in detail, and then we provide qualitative comparisons to Cases 2 and 3.

Fig. 12 shows the distribution of spectral distances between a representative standard, AGV2, and the rest of the spectra in the training set. As expected, most spectra group in packets of four which all correspond to the same standard. The groups of spectra with distances above 80 correspond to DH4912 (nearly pure olivine), MHC2319, and MHC1356 (sulfate standards). Other standards that are distant include gypsums and sediments, while the closest standards include andesites and basalts, as expected.

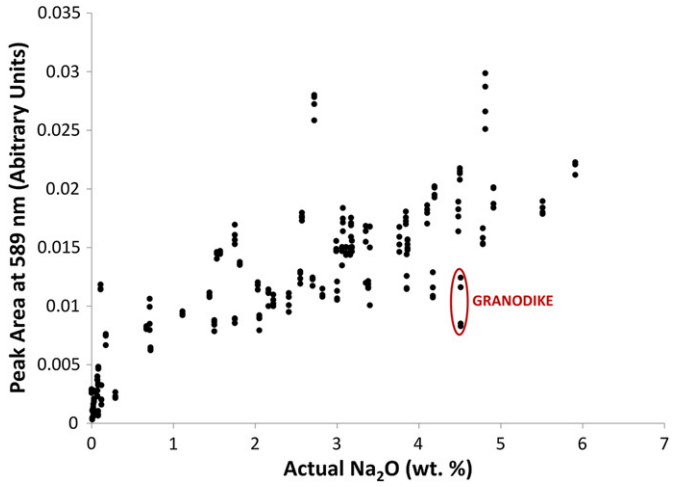

Fig. 11. A plot of the Na emission line intensity at 589.16 nm versus the actual Na_2O content of the standards. Note that Granodike has a relatively low intensity for its Na_2O content, consistent with the underestimate by PLS.

As the outlying spectra are successively removed from the training set, the number of PLS components that corresponds to the optimal RMSEP decreases, as shown in Fig. 13. The initial optimum number of components is large, as this calculation employed a leave-one-spectrum-out rather than the leave-one-standard-out strategy that resulted in the eleven components used to obtain the results in Table 6. The accuracy of the PLS model was calculated after each successive standard removal, and these accuracies are shown in Fig. 14 using two different metrics: the mean of the absolute accuracy and the mean of the relative accuracy of the major elements computed. The absolute accuracy weights the most abundant elements, particularly Si, most heavily, while the relative accuracy weights most heavily the least abundant elements computed, which tend to have the largest relative errors.

The initial part of the curves in both panels in Fig. 14 corresponds to a significant improvement of the PLS model prediction accuracy. Typically, removing 5 to 7 samples improves the prediction accuracy of the PLS model by a factor of about 2. The improvement is better for the absolute accuracy, indicating that the accuracies of the most abundant elements are improved more significantly than the rest. After that improvement, the PLS model prediction errors increase almost monotonously for each sample that is removed from the model, showing, as expected, that a large number of samples is required to provide an adequate model for elemental composition quantitative predictions. The relative accuracy is not optimized for the same number of removed standards for each element. Typically CaO performs better when more standards are removed than for the other elements, preferring the removal of at least 9–12 standards. It is possible that this is due to the very large compositional difference between igneous standards like AGV2 and carbonates, in which CaO comprises a large fraction of the total.

For comparison, the standard-removal test was carried out in reverse, by removing the standards closest to AGV2 in Euclidean space first. In this case, there was essentially no improvement in prediction accuracy, and instead, the general trend was towards steadily increasing errors from the beginning.

Distances from AGV2 were determined by ICA in reduced 10-D space. The same three standards were found to be outliers and the overall distance distribution was very similar to the one obtained by Euclidean calculations in the original space. The optimal number of components once again decreased as the number of samples removed increased. The accuracy of the PLS model as a function of samples removed and the relative accuracy for each element followed similar patterns to those shown in Fig. 14. The same analysis carried out using the Mahalanobis distance in ICA again showed similar results. The Mahalanobis distance appears to be slightly more sensitive to the outliers and the reduction in the optimum number of components as a function of the number of standards removed is somewhat steeper.

A comparison was then made selecting as an unknown the spectrum of a clay standard, SRM97A, which is relatively far from the bulk of the standards, for which basalts and andesites predominate. In this case the only standard in close proximity in Euclidean space was SRM98A, a relatively similar clay standard. In this situation the absolute accuracy of the PLS model does not show any improvement when outlier standards are removed unless about twenty are taken out. The relative accuracy, on the other hand, does show a dip when removing the first few outliers. However, the relative accuracy starts out high in this case because a number of the major elements are near zero wt.% to start with.

Overall, this study shows that removing a few outliers significantly helps the accuracy of those spectra which are near the middle of the distribution of spectra in phase space. However, the current training set is not very large, and removing more than a small number of

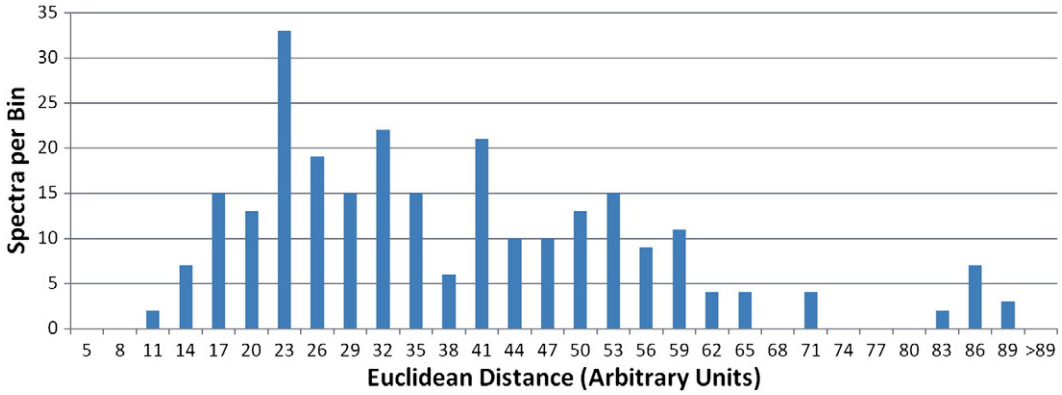

Fig. 12. Histogram showing the number of spectra as a function of Euclidean spectral distance, in arbitrary units, from an AGV2 spectrum, using the full 6144-dimesional space. Each standard is represented by four spectra taken at different points on the powder disks.

outliers results in poorer accuracy and less generalizability to unknown samples.

3.5.3.2. Adding new spectra to the database. As indicated above, a key aspect of the ChemCam spectral database is the ability to remove spectra that are not useful in covering the compositional ranges and, more importantly, to add spectra which more closely represent the range of data from Mars. The original database was built on spectra taken by the flight instrument prior to launch. There are two possibilities for adding new spectra of known compositions after launch and landing. One is to cross-calibrate with the APXS instrument on Mars. This can be done on homogeneous samples for which the difference in sampling size does not matter and for elements for which APXS obtains accurate results, e.g., for Na, Mg, Al, Si, P, S, Cl, K, Ca, Ti, Cr, Mn, Fe, Ni, and Zn [52]. Conversely, APXS cross calibration is not feasible in areas of heterogeneous samples and, more importantly, for elements such as H, Li, Be, B, C, Rb, Sr, Ba that are not generally analyzed by APXS. Although these are not analyzed by PLS, abundances of these elements can be determined by univariate analyses of ChemCam LIBS spectra, when present in sufficient abundances.

Another method of adding spectra to the database is to make LIBS observations on new standards using a surrogate instrument on Earth that matches ChemCam's laser in energy and optical characteristics, and with spectrometers that match the wavelengths and resolutions of ChemCam's. Such instruments were built using flight spare parts and have been installed in laboratories at Los Alamos and Toulouse. It may also be possible to add spectra using slightly less ChemCam-like instruments. To add spectra to the database using any of these instruments one needs to know how accurately each of the instrumental parameters must be matched to ChemCam's. Experience with ChemCam suggests that the spectra are relatively insensitive to the laser energy. We explore the requirements for matching the wavelength and ChemCam's spectral resolution in the next several paragraphs.

To determine the sensitivity of PLS results to the wavelength calibration of the training and test sets, we randomly selected five samples from the cleanroom database to be used as an "unknown" test set. The remaining samples were used to train a PLS model for each of the major elements, with the number of principal components fixed at 15. These models were used to predict the composition of the test set after applying a shift in the wavelength calibration of the test set spectra by up to ± 3 pixels. This shift was applied in increments of 0.05 pixels up to ± 0.25 pixels, after which the shift increment was increased to 0.25 pixels.

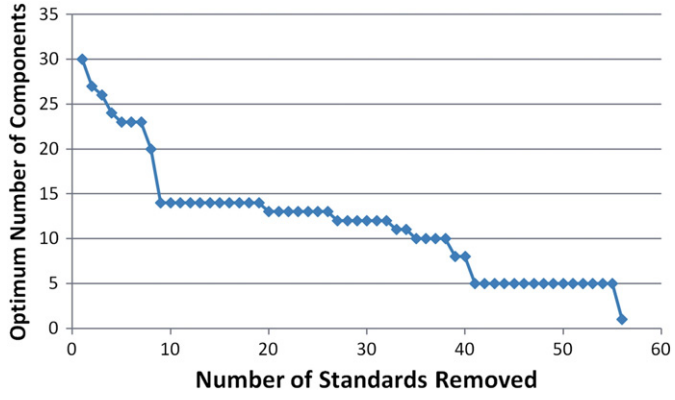

Fig. 13. The number of PLS components that yields the optimal accuracy (lowest RMSEP) as a function of the number of standards removed from the training set.

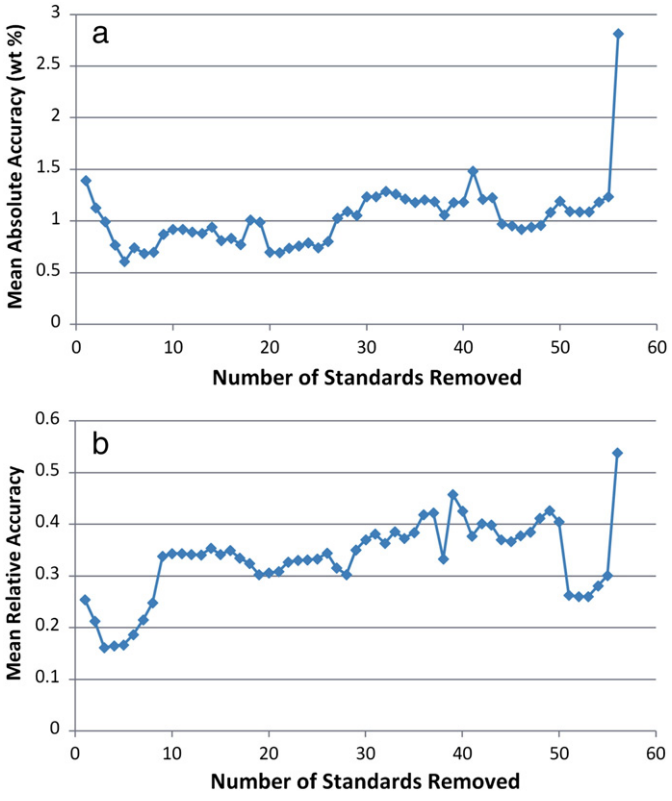

Fig. 14. Accuracy of the composition of AGV2 estimated by PLS as a function of the number of standards removed from the training set. Accuracy is presented both as the mean of the absolute accuracy of the major elements computed (a) and as the mean of the relative accuracy (b), where 0.1 corresponds to 10%.

The calculations were repeated ten times with different sets of five samples held out to serve as the test set. The result of these repeated calculations was a set of ten RMSE curves varying with the magnitude of the wavelength offset for each major element. For each shift increment, we averaged together the ten RMSE values and calculated the standard deviation, resulting in a curve of RMSE values for each element with associated uncertainties (Fig. 15).

The curves show minima at or near zero shift in the wavelength calibration of the test spectra, and the RMSE increases as the offset between the training and test spectra increases. We define acceptable performance as the range of shift values for which the RMSE of the predictions increases by less than 10% relative to the minimum value. By this metric, the maximum absolute mismatch in wavelength calibration that still gave acceptable results was on average ~0.5 pixels.

The asymmetry observed in the average RMSE values in Fig. 15 is likely related to asymmetry of the relevant emission lines. For example, Ti shows a greater increase in error for a negative shift than a positive shift. The most prominent Ti emission lines are in the range of 334 nm to 340 nm, and are broader on the long-wavelength side, consistent with lower errors for positive shifts. The asymmetry in Mn appears to be caused by positive regression coefficients corresponding to the 279.6 nm Mg II emission line in the PLS model. At ChemCam spectral resolution, this line blends with the Mg II line at 279.9 nm, leading to little change in RMSEP for spectra with positive shifts.

We conducted a similar set of calculations to assess the effect of spectral resolution on PLS results, using the same method of selecting a random set of five samples to serve as the test set, and generating PLS models for each element with the number of principal components fixed at 15. In this case, no offset was applied to the wavelength calibration, but the training set spectra were degraded by convolving with a Gaussian with a FWHM of up to 10 pixels. The FWHM was incremented by 0.2 pixels up to a FWHM of 2 pixels, after which it was incremented by 0.5 pixels. Fig. 16 shows the averaged results of ten different test sets.

Again we define acceptable performance as any model for which the RMSEP increases by less than 10% of the original RMSEP. In general, performance is acceptable until the FWHM of the convolved Gaussian is between 1.5 and 2.6 pixels. Al is the most sensitive element to degradation of the training spectra, and this may be caused by the close proximity of the Al I 396.26 nm and Ca II 396.96 lines in the visible portion of the spectra.

3.6. Initial univariate calibrations on Mars

We include here the first results on univariate calibrations on Mars. The rover-mounted CCCTs [21,22] were analyzed periodically during the first 90 days of the MSL mission, in order to check i) the stability of the spectrometers against possible shifts in wavelength-to-channel mapping over a long period or as a function of the spectrometer temperature, and ii) to obtain good statistics on the target compositions. As discussed up to this point, there are two overall methods for determining elemental compositions from the ChemCam spectral data. One method uses multivariate techniques, specifically partial least squares (PLS), to interpolate compositions from a set of standards analyzed by ChemCam prior to launch (see Section 3.5). The PLS results have been used to provide rapid preliminary compositions on the tactical timeline, and rely on the CCCTs for sanity checks. Another method, discussed in Section 3.4, uses calibration of individual peaks to determine abundances. This univariate analysis can take advantage not only of pre-flight calibrations, but can also re-calibrate on Mars using the CCCTs to infer element ratios by ratioing the areas under the appropriate peaks. As discussed extensively in the LIBS literature, each method has advantages and disadvantages. An advantage of the univariate analysis is that it is simpler to implement.

As the ChemCam instrument allows acquisition of LIBS emission spectra on three spectrometers, for most elements there a number of emission lines available to use. The most stable emission lines for major and some trace elements have been selected in order to use

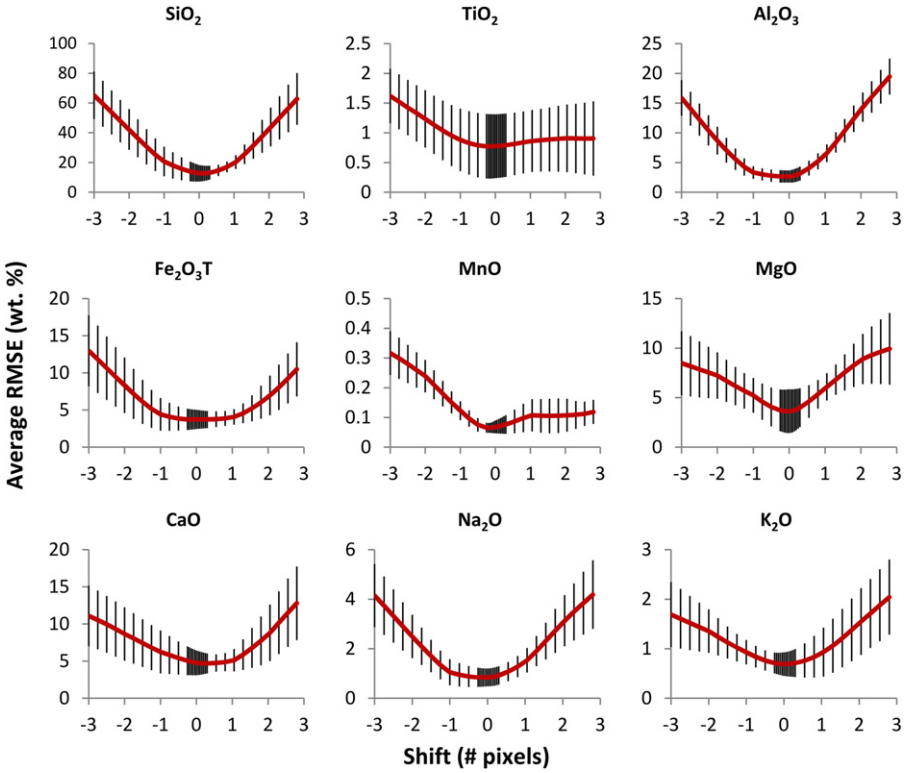

Fig. 15. Average RMSEP for nine major rock-forming elements as the wavelength calibration of the test spectra is shifted by +/−3 pixels. Error bars represent the standard deviation of multiple results using randomly selected test sets.

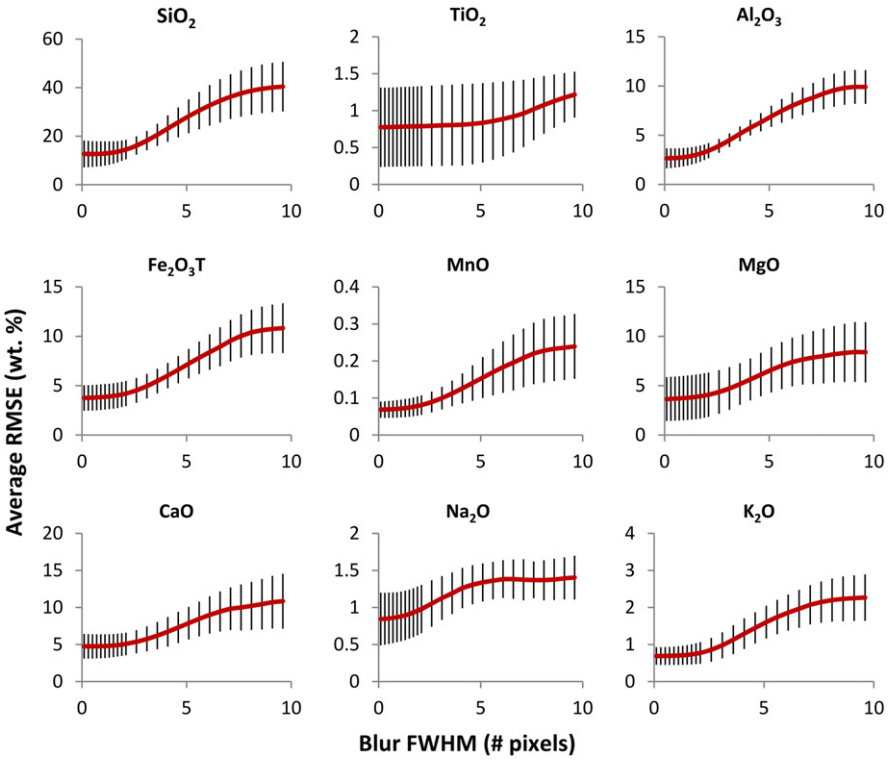

Fig. 16. Average RMSEP for nine major rock-forming elements as the spectral resolution of the training spectra is degraded by convolving with a Gaussian of increasing full-width at half maximum. Error bars represent the standard deviation of multiple results using randomly selected test sets.

the emission areas of the peaks after normalization to the total emission of each spectrum. As noted in Section 3.3, emission is more efficient in the ceramic CCCTs than in the silicate ones, due to a better laser coupling for the ceramics. The results presented here are based on averages of 30 LIBS shots on each observation point on the CCCTs. We have used three sets of CCCT observations performed 27, 76 and 112 Martian days after landing. The selected emission lines are the following (but not all are presented here): 589 and 818 nm for Na, 318 and 422 nm for Ca, 288 and 390 nm for Si, 766 and 770 nm for K, 285 and 448 nm for Mg, 309 nm for Al, and 438 and 404 nm for Fe.

A first approach is to compare emission peak areas versus the known compositions of the CCCTs for all of the major elements. Fig. 17 presents the calibration curve obtained for the Mg peak area. As each CCCT has been observed several times, several points are reported for each set of analyses. Thus, the homogeneity of the CCCT observations is seen in the plot. The results for some of the targets known to be the most homogeneous cluster tightly (i.e., norite, picrite, with a relative standard deviation less than 10%), but scattered points are more typical of heterogeneous targets, as seen for KGA-MED-S and NAU2-LO-S (Fig. 17). However, all of the tested calibration curves present fairly good correlation coefficients, even for those with the highest heterogeneity in the CCCT. Thus, for each element peak area it is possible to obtain an estimate of the elemental content for each LIBS analysis.

As geologists frequently use element ratios for comparisons, univariate analyses were also tested for this specific aspect. This element ratio approach is also classically used by the LIBS community because their use avoids the problem of differences in overall signal intensity between samples. Fig. 18 shows that for Al/Si, all of the CCCTs plot close to the regression line, giving an R^2 of 0.92. In all cases, the

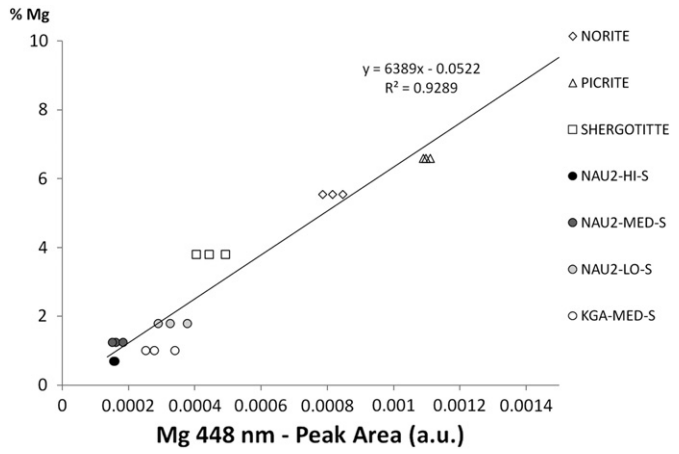

Fig. 17. Univariate calibration curve obtained on Mars data for Mg using the 448 nm emission line, using CCCT observations from three different days.

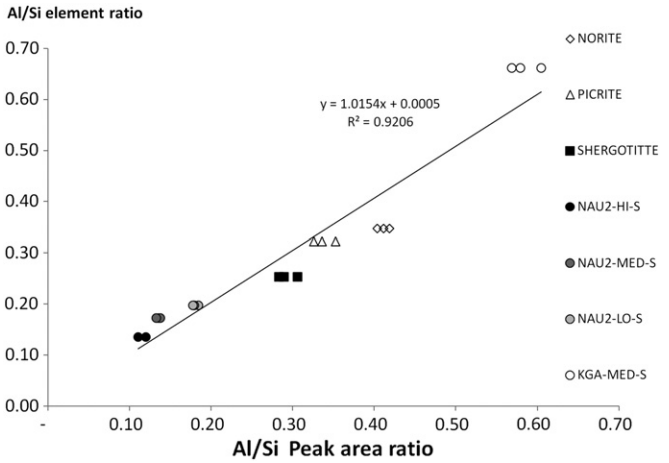

Fig. 18. Univariate calibration of Al/Si ratios using the 309 nm Al and 288 nm Si emission lines observed on the CCCTs on three different days on Mars.

element ratio curves present better correlation coefficients than those obtained for direct peak area curves.

Using three sets of CCCT analyses, we have obtained the first univariate calibration curves from Mars. Using these data avoids the use of instrument response correction on Mars and is not subject to instrument transmission changes between Earth and on Mars. To improve calibration curve correlation coefficients we must acquire more LIBS analyses of the CCCTs. It is clear that both univariate and multivariate analyses will be used to determine compositions of samples on Mars.

4. Conclusions

The ChemCam instrument on the Curiosity Mars rover represents a significant effort to develop a highly efficient tool for assessing Mars surface compositions at stand-off distances and with the capability to profile into rocks and soils. The work described here on ChemCam LIBS calibration is the largest effort to date to investigate quantitative applications of remote LIBS for geological field work. A set of 69 rock powder standards was used to characterize the instrument performance. The standards are described in terms of physical characteristics, elemental abundances, and in most cases, mineral composition. We give an overview on the strategy for overall analysis of the ChemCam data. This strategy focuses on using univariate analyses for trace element detection and quantification, and multivariate analyses, supported by univariate analyses, for the major elements. We describe the data processing steps to produce Level-1 LIBS data products. The coupling efficiency of potential targets varies by a factor of nearly 30, and the relative coupling efficiencies are described. ChemCam detection limits are investigated, showing, for example, that lithium can be not only detected, but quantified with as little as 25 ppm.

The ChemCam LIBS calibration training set was developed and built before the field site (Gale crater on Mars) was selected, so it had to be quite general to start with, but the methods needed to be adaptable to the initial findings. We have shown that such a training set can be built, and that the training set can be later adapted both by culling outliers that turn out to not be needed and, in the near future, by adding to additional standards as initial findings dictate. It is shown that a larger training set is strongly desirable, and it is shown that samples near the center of the compositional phase space could be trained with a smaller set than samples near the edge of the phase space. In anticipation of adding standards to the training set by using spectra obtained on laboratory instruments nearly identical to ChemCam, requirements are determined for matching the wavelength at each channel and for matching ChemCam's spectral resolution. It is shown that errors associated with precision are only a small fraction of the overall uncertainties. We have also shown that, preliminarily and within current uncertainties, the plasma temperature does not appear to change as a function of the distance to the target. Overall, the calibration database obtained with the ChemCam instrument prior to launch has supported the Mars analyses moderately well, but will be enlarged and further optimized for the Mars data that are currently being obtained.

Acknowledgments

The ChemCam team is grateful for support from the NASA Mars Program Office for ChemCam, and from CNES. We also gratefully acknowledge the Los Alamos National Laboratory's laboratory-directed research and development exploratory research (LDRD-ER) program for supporting early MVA studies. Many people supported the ChemCam instrument that was used to carry out these studies, and we are particularly grateful to other ChemCam team members who supported this work. B. Banisadr is thanked for his contributions to the total emission studies.

Appendix A. Supplementary data

Supplementary data to this article can be found online at http://dx.doi.org/10.1016/j.sab.2013.02.003.

References

[1] R.C. Wiens, S. Maurice, B. Barraclough, M. Saccoccio, W.C. Barkley, J.F. Bell III, et al., The ChemCam instruments on the Mars Science Laboratory (MSL) rover: body unit and combined system performance, Space Sci. Rev. (2012), http://dx.doi.org/10.1007/S11214-012-9902-4.
[2] S. Maurice, R.C. Wiens, M. Saccoccio, B. Barraclough, O. Gasnault, O. Forni, et al., The ChemCam instruments on the Mars Science Laboratory (MSL) rover: science objectives and mast unit, Space Sci. Rev. 170 (2012) 95–166.
[3] D.W. Hahn, N. Omenetto, Laser-induced breakdown spectroscopy (LIBS), part I: review of basic diagnostics and plasma–particle interactions: still-challenging issues within the analytical plasma community, Appl. Spectrosc. 64 (2010) 335A–366A.
[4] D.W. Hahn, N. Omenetto, Laser-induced breakdown spectroscopy (LIBS), part II: review of instrumental and methodological approaches to material analysis and applications to different fields, Appl. Spectrosc. 66 (2012) 347–419.
[5] D. Cremers, L.J. Radziemski, Handbook of Laser Induced Breakdown Spectroscopy, Wiley, New York, 2006. (302 pp.).
[6] A.K. Knight, N.L. Scherbarth, D.A. Cremers, M.J. Ferris, Characterization of laser-induced breakdown spectroscopy (LIBS) for application to space exploration, Appl. Spectrosc. 54 (2000) 331–340.
[7] A.S. Eppler, D.A. Cremers, D.D. Hickmott, M.J. Ferris, A.C. Koskelo, Matrix effects in the detection of Pb and Ba in soils using laser-induced breakdown spectroscopy, Appl. Spectrosc. 50 (1996) 1175–1181.
[8] A. Ciucci, V. Palleschi, S. Rastelli, A. Salvetti, D.P. Singh, E. Tognoni, CF-LIPS: a new approach to LIBS spectra analysis, Laser Part. Beams 17 (1999) 793–797.
[9] D. Bulajic, M. Corsi, G. Cristoforetti, S. Legnaioli, V. Palleschi, A. Salvetti, E. Tognoni, A procedure for correcting self-absorption in calibration free-laser induced breakdown spectroscopy, Spectrochim. Acta Part B 57 (2002) 339–353.
[10] M. Dell'Aglio, A. De Giacomo, R. Gaudioso, O. De Pascale, G.S. Senesi, S. Longo, Laser induced breakdown spectroscopy applications to meteorites: ChemCam analysis and composition profiles, Geochim. Cosmochim. Acta 74 (2010) 7329–7339.
[11] J.-B. Sirven, B. Bousquet, L. Canioni, L. Sarger, Laser-induced breakdown spectroscopy of composite samples: comparison of advanced chemometrics methods, Anal. Chem. 78 (2006) 1462–1469.
[12] S.M. Clegg, R.C. Wiens, J.E. Barefield, E. Sklute, M.D. Dyar, Quantitative remote laser induced breakdown spectroscopy by multivariate analysis, Spectrochim. Acta Part B 64 (2009) 79–88.
[13] J.M. Tucker, M.D. Dyar, M.W. Schaefer, S.M. Clegg, R.C. Wiens, Optimization of laser-induced breakdown spectroscopy for rapid geochemical analysis, Chem. Geol. 277 (2010) 137–148.
[14] M.D. Dyar, J.M. Tucker, S. Humphries, S.M. Clegg, R.C. Wiens, M.D. Lane, Strategies for Mars remote laser-induced breakdown spectroscopy analysis of sulfur in geological samples, Spectrochim. Acta Part B 66 (2010) 39–56.
[15] M.D. Dyar, M.L. Carmosino, E.A. Speicher, M.V. Ozanne, S.M. Clegg, R.C. Wiens, Comparison of partial least squares and LASSO regression techniques for laser-induced breakdown spectroscopy data of geological samples, Spectrochim. Acta Part B 70 (2012) 51–67.
[16] R.B. Anderson, R.V. Morris, S.M. Clegg, J.F. Bell III, R.C. Wiens, S.D. Humphries, S.A. Mertzman, T.G. Graff, R. McInroy, The influence of multivariate analysis methods and target grain size on the accuracy of remote quantitative chemical analysis of rocks using laser induced breakdown spectroscopy, Icarus 215 (2011) 608–627.
[17] R.B. Anderson, J.F. Bell III, R.C. Wiens, R.V. Morris, S.M. Clegg, Clustering and training set selection methods for improving the accuracy of quantitative laser induced breakdown spectroscopy, Spectrochim. Acta Part B 70 (2012) 24–32.
[18] K. Govindaraju, 1994 compilation of working values and sample description for 383 geostandards, Geostand. Newslett. 18 (1994) 1–158.
[19] K.P. Jochum, U. Nohl, K. Herwig, E. Lammel, B. Stoll, A. Hofmann, GeoReM: a new geochemical database for reference materials and isotopic standards, Geostand. Geoanal. Res. 29 (2005) 333–338.
[20] K.P. Jochum, J. Enzweiler, R. Mertz-Kraus, X. Wang, GGR biennial review: reference materials in geoanalytical and environmental research—review for 2008 and 2009, Geostand. Geoanal. Res. 34 (2010) 353–385.
[21] C. Fabre, S. Maurice, A. Cousin, R.C. Wiens, O. Forni, V. Sautter, D. Guillaume, Onboard calibration igneous targets for the Mars Science Laboratory Curiosity rover and the chemistry camera laser induced breakdown spectroscopy instrument, Spectrochim. Acta Part B 66 (2011) 280–289.
[22] D. Vaniman, M.D. Dyar, R.C. Wiens, A. Ollila, N. Lanza, J. Lasue, M. Rhodes, S.M. Clegg, Ceramic ChemCam calibration targets on Mars Science Laboratory, Space Sci. Rev. 170 (2012) 229–255.
[23] M. Pichavant, D.J. Kontak, J. Valencia-Herrera, The Miocene–Pliocene Macusani Volcanics, SE Peru. I. Mineralogy and magmatic evolution of a two-mica aluminosilicate-bearing ignimbrite suite, Contrib. Mineral. Petrol. 100 (1988) 300–324.
[24] M. Pichavant, D.J. Kontak, L. Briqueu, J. Valencia-Hererra, A.H. Clark, The Miocene–Pliocene Macusani Volcanics, SE Peru. II. Geochemistry and origin of a felsic peraluminous magma, Contrib. Mineral. Petrol. 100 (1988) 325–338.
[25] B.C. Clark, R.V. Morris, S.M. McLennan, R. Gellert, B. Jolliff, A.H. Knoll, S.W. Squyres, T.K. Lowenstein, D.W. Ming, N.J. Tosca, A. Yen, P.R. Christensen, S. Gorevan, J.

Brückner, W. Calvin, G. Dreibus, W. Farrand, G. Klingelhoefer, H. Waenke, J. Zipfel, J.F. Bell III, J. Grotzinger, H.Y. McSween, R. Rieder, Chemistry and mineralogy of outcrops at Meridiani Planum, Earth Planet. Sci. Lett. 240 (2005) 73–94.
[26] J. Kemp, R. Redemann, Geology of the Elizabethtown and Port Henry quadrangles, N.Y. State Mus. Bull. 138 (1910) 173.
[27] R.V. Morris, S.W. Ruff, R. Gellert, D.W. Ming, R.E. Arvidson, B.C. Clark, D.C. Golden, K. Siebach, G. Klingerhöfer, C. Schröder, I. Fleischer, A.S. Yen, S.W. Squyres, Identification of carbonate-rich outcrops on Mars by the Spirit rover, Science 239 (2010) 421–424.
[28] J.L. Campbell, A.M. McDonald, G.M. Perrett, S.M. Taylor, A GUPIX-based approach to interpreting the PIXE-plus-XRF spectra from the Mars Exploration Rovers: II geochemical reference materials, Nucl. Instrum. Meth. B269 (2011) 69–81.
[29] S. Mallat, A Wavelet Tour of Signal Processing, 2nd ed. Academic Press, 1999.
[30] J.-L. Starck, F. Murtagh, Astronomical Image and Data Analysis, Springer, Berlin, 2006.
[31] A. Kramida, Y. Ralchenko, J. Reader, NIST ASD Team, NIST Atomic Spectra Database (Ver. 5.0), National Institute of Standards and Technology, Gaithersburg, MD, 2012. (Online. Available: http://physics.nist.gov/asd, 2013, February 3).
[32] R. Brennetot, J.-L. Lacour, E. Vors, A. Rivoallan, D. Vailhen, S. Maurice, Mars analysis by laser-induced breakdown spectroscopy (MALIS): influence of Mars atmosphere on plasma emission and study of factors influencing plasma emission with the use of Doehlert designs, Appl. Spectrosc. 57 (2003) 744–752.
[33] J.A. Aguilera, C. Aragon, Characterization of a laser-induced plasma by spatially resolved spectroscopy of neutral atom and ion emissions: comparison of local and spatially integrated measurements, Spectrochim. Acta Part B 59 (2004) 1861–1876.
[34] S. Yalcin, D.R. Crosley, G.P. Smith, G.W. Faris, Influence of ambient conditions on the laser air spark, Appl. Phys. 68 (1999) 121–130.
[35] M. Sabsabi, P. Cielo, Quantitative analysis of aluminum alloys by laser-induced breakdown spectroscopy and plasma characterization, Appl. Spectrosc. 49 (1995) 499–507.
[36] G. Cristoforetti, A. De Giacomo, M. Dell'Aglio, S. Legnaioli, E. Tognoni, V. Palleschi, N. Omenetto, Local thermodynamic equilibrium in laser-induced breakdown spectroscopy: beyond the McWhirter criterion, Spectrochim. Acta Part B 65 (2010) 86–95.
[37] B. Sallé, J.-L. Lacour, P. Mauchien, P. Fichet, S. Maurice, G. Manhes, Comparative study of different methodologies for quantitative rock analysis by laser-induced breakdown spectroscopy in a simulated Martian atmosphere, Spectrochim. Acta Part B 61 (2006) 301–313.
[38] J. Lasue, R.C. Wiens, S.M. Clegg, D.T. Vaniman, K.H. Joy, S. Humphries, A. Mezzacappa, N. Melikechi, R.E. McInroy, S. Bender, Laser induced breakdown spectroscopy (LIBS) for lunar exploration, J. Geophys. Res. Planets 117 (2012) E01002, http://dx.doi.org/10.1029/2011JE003898.
[39] L.A. Currie, Limits for qualitative detection and quantitative determination. Application to radiochemistry, Anal. Chem. 40 (1968) 586–593.
[40] D.L. Massart, B.G.M. Vandeginste, L.M.C. Buydens, S. De Jong, P.J. Lewi, J. Smeyers-Verbeke, Handbook of Chemometrics and Qualimetrics: Part A, Elsevier, New York, 1998.
[41] B. Sallé, J.-L. Lacour, E. Vors, P. Fichet, S. Maurice, D.A. Cremers, R.C. Wiens, Laser-induced breakdown spectroscopy for Mars surface analysis: capabilities at stand-off distance and detection of chlorine and sulfur elements, Spectrochim. Acta Part B 59 (2004) 1413–1422.
[42] A. Gonzalez, M. Ortiz, J. Campos, Determination of sulfur contents in steel by laser-produced plasma atomic emission spectroscopy, Appl. Spectrosc. 49 (1995) 1632–1635.
[43] L. Dudragne, P. Adam, J. Amourouz, Time-resolved laser-induced breakdown spectroscopy: application for qualitative and quantitative detection of fluorine, chlorine, sulfur, and carbon in air, Appl. Spectrosc. 52 (1998) 1321–1327.
[44] A.M. Ollila, J.G. Blank, R.C. Wiens, J. Lasue, H.E. Newsom, S.M. Clegg, A. Cousin, S. Maurice, Preliminary results on the capabilities of the ChemCam laser-induced breakdown spectroscopy (LIBS) instrument to detect carbon on Mars, Lunar Planet. Sci. XLII (2011) 2395.
[45] R. Bro, Multi-way calibration. Multilinear PLS, J. Chemom. 10 (1996) 47–61.
[46] R.S. Bricklemyer, D.J. Brown, J.E. Barefield, S.M. Clegg, Intact soil core total, inorganic, and organic carbon measurement using laser-induced breakdown spectroscopy, Soil Sci. Soc. Am. J. 75 (2011) 1006–1018.
[47] A. Cousin, V. Sautter, C. Fabre, S. Maurice, R.C. Wiens, Textural and modal analyses of picritic basalts with ChemCam laser-induced breakdown spectroscopy, J. Geophys. Res. Planets 117 (2012) E10002, http://dx.doi.org/10.1029/2012JE004132.
[48] P. Comon, Independent component analysis, in: J.L. Lacoume (Ed.), Higher-Order Statistics, Elsevier, Amsterdam, 1992, pp. 29–38.
[49] P. Comon, Independent component analysis, a new concept? Signal Process. 36 (1994) 287–314.
[50] O. Forni, S. Clegg, R.C. Wiens, S. Maurice, O. Gasnault, Multivariate analyses of ChemCam first calibration samples, Lunar Planet. Sci. XL (2009) 1523.
[51] A. Cousin, O. Forni, S. Maurice, J. Lasue, O. Gasnault, R. Wiens, the ChemCam team, Independent component analysis classification for ChemCam remote sensing data, Lunar Planet. Sci. XLII (2011) 1973.
[52] J.L. Campbell, G.M. Perrett, R. Gellert, S.M. Andrushenko, N.I. Boyd, J.A. Maxwell, P.L. King, C.D.M. Schofield, Calibration of the Mars Science Laboratory alpha particle X-ray spectrometer, Space Sci. Rev. 170 (2012) 319–340.